Direct numerical simulation of the interaction between a shock wave and various types of isotropic turbulence

S. Jamme, J.-B. Cazalbou, F. Torres and P. Chassaing
ENSICA, 1 Place Emile Blouin, 31056 Toulouse cedex 5, France

June 22, 2002

Abstract. Direct Numerical Simulation (DNS) is used to study the interaction between normal shock waves of moderate strength ($M_1 = 1.2$ and $M_1 = 1.5$) and isotropic turbulence. A complete description of the turbulence behaviour across the shock is provided and the influence of the nature of the incoming turbulence on the interaction is investigated. The presence of upstream entropy fluctuations satisfying the Strong Reynolds Analogy enhances the amplification of the turbulent kinetic energy and transverse vorticity variances across the shock compared to the solenoidal (pure vorticity) case. Budgets for the fluctuating-vorticity variances are computed, showing that the baroclinic torque is responsible for this additional production of transverse vorticity. More reduction of the transverse Taylor microscale and integral scale is also observed in the vorticity-entropy case while no influence can be seen on the longitudinal Taylor microscale. When the upstream turbulence is dominated by acoustic and vortical fluctuations, less amplification of the kinetic energy (for Mach numbers between 1.25 and 1.8), less reduction of the transverse microscale and more amplification of the transverse vorticity variance are observed through the shock compared to the solenoidal case. In all cases, the classic estimation of Batchelor relating the dissipation rate and the integral scale of the flow proves to be invalid. These results are obtained with the same numerical tool and similar flow parameters, and they are in good agreement with Linear Interaction Analysis (LIA).

Keywords: DNS, shock/turbulence interaction, compressible turbulence, linear analysis.

1. Introduction

For transonic and supersonic flows of engineering interest, the coexistence of shock waves with some background turbulence is an almost unavoidable feature. Shock-boundary-layer interactions or supersonic over-expanded jets are obvious examples that cumulate so much complicating effects (anisotropy of the background turbulence, mean-flow gradients, oblique or bent shock wave, unsteady separation etc.) that a detailed understanding remains far from reach. For this reason, several studies have focused on the interaction between isotropic turbulence and a normal shock wave as one of the basic phenomena involved in these flows. For most of these studies, the description of compressible turbulence is based on Kovasznay's modal decomposition [23] in terms of rotational, entropic and acoustic modes and the main issue is to understand how the proportions of these modes in the incoming turbulence may influence the way it is modified when passing through the shock.

Initial investigations on the subject were theoretical and based on linear analysis. The Linear Interaction Analysis (LIA) was developed by Ribner [35–37], Moore [33] and recently revisited and completed by Lee, Lele and Moin [25, 27], Mahesh, Lele and Moin [30, 32] and Fabre *et al.* [8, 9]. It may be used when the turbulent fluctuations are small compared to mean values and when rapid changes occur to the flow. This is the case in shock-turbulence interaction where the time required for the upstream turbulent flow to pass through the shock is small compared to the turbulent time scale. The basic principle of LIA consists in solving the linearized Euler equations behind the shock wave, the boundary conditions at the shock being expressed in terms of the upstream disturbances by the use of the Rankine-Hugoniot relations.

It shows that an elementary wave corresponding to one of Kovasznay's modes is refracted through the shock and generates one wave of each of the other two modes. Amplitudes, length scales and orientations of the refracted and generated waves can be determined as functions of those of the incoming wave and some transfer functions that depend on the upstream Mach number and incident angle of the incoming wave. Since upstream homogeneous turbulence may be approximated by a superposition (spectrum) of elementary waves which are independent in the inviscid linear limit (*i.e.* up to first order), modification of turbulence through the shock wave can be described from the sum of the downstream elementary waves. Despite the fact that nonlinear and viscous mechanisms are neglected in the analysis, LIA provides accurate description of the essential characteristics of the interaction:

- amplification of the different components of the turbulent kinetic energy, as well as rms values of the fluctuating pressure, temperature and density;
- generation of anisotropy behind the shock, with a non-monotonic evolution of the streamwise normal Reynolds stress and an amplification of the transverse fluctuating vorticity;
- reduction of the Taylor microscales;
- significant production of entropy fluctuations behind the shock when the upstream Mach number is higher than 1.2.

The influence of the nature – in terms of Kovasznay's decomposition – of the incoming turbulence can also be investigated and shows that:

- Compared to a pure solenoidal turbulent flow, velocity and vorticity fluctuations are more (resp. less) amplified through the shock

when entropy fluctuations corresponding to a negative (resp. positive) correlation between the longitudinal velocity and temperature fluctuations are present upstream of the shock. In an interpretation based on linear considerations, Mahesh *et al.* [32] attributed this phenomenon to the action of the baroclinic torque in the equations of the fluctuating-vorticity variances. Another consequence of the presence of entropy fluctuations upstream is more (resp. less) reduction of the transverse Taylor microscale when the velocity-temperature correlation is negative (resp. positive).

– When the acoustic mode is present upstream, velocity fluctuations are less amplified than in the solenoidal case for low Mach numbers, whereas the opposite is observed for Mach numbers greater than 3.

Rapid Distortion Theory (RDT) has also been applied to the problem of shock-turbulence interaction (see e.g. Jacquin *et al.* [19]). However, this work showed that RDT leads to a large overestimation of the turbulent kinetic energy at high Mach numbers. A key point is that the compression of a turbulent field by a shock wave is rapid, but inhomogeneous, whereas RDT describes a homogeneous compression and is not based on the Rankine-Hugoniot jump conditions. Consequently, the warping of the shock front due to the interaction with the incident turbulent field is not taken into account by RDT and the nature of the downstream perturbation field is not correctly predicted by this theory. This makes RDT unsuited for accurately predicting shock/turbulence interactions, whereas LIA is much closer to the physics of the problem.

Since the early 90's, Direct Numerical Simulation (DNS) and Large-Eddy Simulation (LES) have been applied to the problem of shock-turbulence interaction (Rotman [38], Lee *et al.* [27, 28], Hannappel and Friedrich [13], Mahesh *et al.* [32], Ducros *et al.* [6], Garnier *et al.* [10, 11],

Dubois *et al.* [5]). Although limited to low Reynolds numbers, these studies mostly confirm the LIA results. In addition, the availability of all the terms in the budget equations for the main statistics (turbulent kinetic energy, normal Reynolds stresses, fluctuating vorticity) also helps to elucidate the basic mechanisms responsible for their behaviour during the interaction. Amplification of turbulence and generation of anisotropy just behind the shock, for instance, have been found to rely on the action of the pressure-dilatation and pressure-diffusion terms in the Reynolds-stress transport equations (see Ref. [27]).

Experiments on the interaction are difficult to perform but have nevertheless been conducted either in wind tunnels or shock tubes by several authors. In supersonic wind tunnels [1, 4, 18, 20], steady shocks can be created with appropriate shock-generating devices. A grid-type turbulence generator is usually used to produce homogeneous, quasi-isotropic turbulence. The measurements are made at various axial positions downstream of the shock wave. Statistics of the flow are thus determined as a function of the distance between the measurement point and the shock wave. These experiments are easy to compare with numerical simulations since the shock is steady. This is not the case with shock-tube experiments [3, 15–17, 22], where a travelling shock wave passes through a grid, producing homogeneous turbulence with constant mean velocity. This turbulent field will interact with the shock wave after reflection of the latter on the end wall of the tube. Statistical measurements are performed at a fixed position in the tube. Since the distance between the probe and the propagating shock wave changes during the useful period of measurements, the results of these experiments are not easy to compare with numerical simulations or wind-tunnel experiments. Another difficulty is the relatively short time available for the measurements depending on the dimension of the

shock tube and the shock intensity. From a general point of view, all these experimental results are subject to specific types of uncertainties due, for instance, to the finite particle response that affects LDA measurements in compressible flows or small variation of the mean velocity downstream of the shock; and information concerning the precise nature of the incident turbulence usually lacks. However, the data agree with the DNS and LIA results for the evolutions of the main statistics across the shock; but contradictions still exist concerning the behaviour of turbulent microscales during the interaction: apart from Barre *et al.* [1], experimental data show an overall increase of the microscales during the interaction, in contradiction with theory and simulation.

In the present work, DNS is used to compare the evolution across the same shock wave of three different turbulent flows generated using Kovasznay's decomposition. These comparisons are provided for two different values of the upstream Mach number and for a turbulent Mach number significantly higher than in previous studies. Details on the flow parameters are given in Table I, together with those used in the previous works cited above. It can be seen that the interaction with different types of incoming turbulence has been quite well covered, but significant differences exist in the flow parameters used by the different authors. Here, simulations with three types of incoming turbulence are performed with the same numerical tool and flow parameters to ensure that the observed differences only depend on the nature of the upstream turbulence. The latest developments of LIA were also reproduced with the same conditions [21], to allow systematic comparison with the simulation results.

The paper is organised as follows. Section 2 gives a description of the problem and provides details concerning the numerical tool and the incoming turbulence. Results from the simulations and analysis are

presented in Section 3: the main features of the interaction are first described with a reference case, then the influence of upstream entropy and pressure fluctuations is addressed.

2. Numerical approach

2.1. Mathematical model

We consider a Newtonian fluid with constant physical properties: R is its perfect-gas constant, and c_p and c_v its specific heats with $\gamma = c_p/c_v$. The fluid thermal conductivity and dynamic viscosity depend on the temperature and will be denoted as κ^* and μ^* (the asterisk as a superscript indicates a dimensional variable or function). The flow is governed by the Navier-Stokes equations, written here in their most general form as

$$\frac{\partial \rho^*}{\partial t^*} + \frac{\partial}{\partial x_i^*}(\rho^* u_i^*) = 0,$$

$$\frac{\partial}{\partial t^*}(\rho^* u_i^*) + \frac{\partial}{\partial x_j^*}(\rho^* u_i^* u_j^* + p^* \delta_{ij}) - \frac{\partial \tau_{ij}^*}{\partial x_j^*} = 0,$$

$$\frac{\partial}{\partial t^*}(\rho^* E^*) + \frac{\partial}{\partial x_i^*}\left((\rho^* E^* + p^*) u_i^*\right) - \frac{\partial}{\partial x_j^*}\left(u_i^* \tau_{ij}^*\right) + \frac{\partial q_i^*}{\partial x_i^*} = 0,$$

with:

$$\tau_{ij}^* = \mu \left(\frac{\partial u_i^*}{\partial x_j^*} + \frac{\partial u_j^*}{\partial x_i^*} - \frac{2}{3} \frac{\partial u_k^*}{\partial x_k^*} \delta_{ij} \right) \quad \text{and} \quad q_i^* = -\kappa \frac{\partial T^*}{\partial x_i^*}.$$

In these equations, u_i^* is the velocity component along x_i^*; ρ^*, p^* and T^* are, respectively, the fluid density, pressure and temperature; and E^* is the total energy per unit mass ($E^* = c_v T^* + u_i^* u_i^*/2$). The system is closed with the perfect-gas law $p^* = \rho^* R T^*$.

In the interaction problem, the upstream flow is defined by the fluid density (ρ_1^*), temperature (T_1^*) and Mach number ($M_1 > 1$). Adequate counterpressure downstream causes the normal shock to form. A fluctuating field is then superposed onto the upstream flow and advected through the shock. It is characterized by the initial Taylor microscale (λ_0^*) and rms value of the velocity fluctuation in the direction of the flow (u_0^*). We use ρ_1^*, T_1^*, u_0^* and $2 \times \lambda_0^*$ to scale all variables and functions [except viscosity, scaled by $\mu_1^* = \mu^*(T_1^*)$] and recast the problem in the following nondimensional form:

$$\frac{\partial \rho}{\partial t} + \frac{\partial}{\partial x_i}(\rho u_i) = 0, \tag{1}$$

$$\frac{\partial}{\partial t}(\rho u_i) + \frac{\partial}{\partial x_j}(\rho u_i u_j + p\,\delta_{ij}) - \frac{\partial \tau_{ij}}{\partial x_j} = 0, \tag{2}$$

$$\frac{\partial}{\partial t}(\rho E) + \frac{\partial}{\partial x_i}\left((\rho E + p) u_i\right) - \frac{\partial}{\partial x_j}\left(u_i \tau_{ij}\right) + \frac{\partial q_i}{\partial x_i} = 0, \tag{3}$$

with:

$$\begin{aligned}
\tau_{ij} &= \frac{\mu}{Re_r}\left(\frac{\partial u_i}{\partial x_j} + \frac{\partial u_j}{\partial x_i} - \frac{2}{3}\frac{\partial u_k}{\partial x_k}\delta_{ij}\right), \\
q_i &= -\frac{\mu}{(\gamma - 1)\, M_r^2\, Re_r\, Pr}\,\frac{\partial T}{\partial x_i}, \\
p &= \frac{\rho T}{\gamma M_r^2}, \\
E &= \frac{p}{\rho(\gamma - 1)} + \frac{1}{2}\, u_i u_i.
\end{aligned}$$

Then, the problem is uniquely defined by the values of the reference parameters:

$$Re_r = \frac{2\,\rho_1^*\, u_0^*\, \lambda_0^*}{\mu_1^*}, \quad M_r = \frac{u_0^*}{(\gamma R\, T_1^*)^{1/2}}, \quad Pr = \frac{\mu_1^* c_p}{\kappa_1^*},$$

and the nondimensional value of the upstream velocity $U_1 = M_1/M_r$. The Prandtl number is assumed to be constant, and viscosity is allowed to vary with temperature through Sutherland's formula:

$$\mu = T^{3/2}\frac{1+C}{T+C}.$$

From now on we shall consider that the fluid is air with the following values of the constants:

$$\gamma = 1.4,\ Pr = 0.7,\ \text{and}\ C = 0.414\ \text{for}\ T_1^* = 273\ \text{K}.$$

2.2. Numerical model

Equations (1)–(3) are numerically solved on a cubic domain – sketched in Figure 1 – the size of which is 2π in the three directions. The mean flow is aligned with x_1, and periodic conditions are specified in the two other directions. At each time step, velocity, pressure, temperature, and density fields are specified at the inflow. These fields are superpositions of a uniform mean flow [$\overline{\mathbf{u}} = U_1\,\mathbf{x}_1$, $\overline{p} = 1/(\gamma M_r^2)$, $\overline{T} = 1$, $\overline{\rho} = 1$, where the overbar denotes the conventional Reynolds average] and turbulent fluctuations (denoted further by a prime) in velocity, pressure, temperature, and density. The outflow is subsonic, and the first-order characteristic boundary conditions of Thompson [40, 41] are used. At the beginning of the calculation, a plane shock wave at Mach number M_1 is specified in the middle of the computational domain; the flow is steady and homogeneous on each side of the shock, satisfying the Rankine-Hugoniot relations.

The numerical solution of Equations (1)–(3) is based on a finite-volume version of the explicit predictor-corrector MacCormack scheme [29], which is second-order accurate in space and time. At each time

step, forward or backward approximations are used in turn for the inviscid part of the flux vector, and centered approximations are used for the viscous terms. Calculations have been performed for $M_1 = 1.2$ and $M_1 = 1.5$. In all cases, the value of the time step has been chosen so as to satisfy the Courant-Friedrichs-Lewy criterion for explicit schemes (CFL $= 0.8 < 1$). The numerical grid is made of 128 points with a constant spacing in the two homogeneous directions. In the streamwise direction, the grid *must* allow the "viscous shock" to be resolved. At Mach number 1.2, 128 points with a constant spacing were found sufficient (11 points in the *finite* width of the shock), but 210 points and stretching were needed to resolve the shock at Mach number 1.5 (15 points in the *finite* width of the shock). Note that viscosity removes the shock discontinuity, so that the viscous problem has a smooth (regular) solution, and the numerical scheme keeps its order of accuracy through the shock.

Validation of the numerical code was carefully conducted. Extensive details about this validation can be found in the appendix.

2.3. Incoming turbulence

The turbulent data superposed onto the mean flow at the upstream boundary of the computational domain correspond to several developed turbulent fields obtained from preliminary simulations of time-decaying isotropic turbulence. They are advected through the boundary using Taylor's hypothesis. This hypothesis is questionable for compressible turbulence, but Lee *et al.* [26] showed that it remains valid for moderate turbulent Mach numbers and turbulence intensities ($M_t < 0.5$ and $u'_{1\,\mathrm{rms}}/\overline{u}_1 < 0.15$, where $M_t = q/\overline{c} = (\overline{u'_i u'_i})^{1/2}/\overline{c}$ and $\overline{c}$ is the speed of sound), which is the case here.

The procedure used to generate the incoming fluctuating fields allowed us to study the interaction of three different kinds of homogeneous isotropic turbulence with the shock. Three kinds of input data were therefore generated, dominated respectively by:

- vorticity fluctuations (solenoidal mode);
- vorticity and entropy fluctuations (solenoidal/entropy mode);
- vorticity and pressure fluctuations (solenoidal/acoustic mode).

In all cases, a cubic domain of $(2\pi)^3$ discretized with an equidistant grid of 128^3 points is initialized with a random velocity field generated with the algorithm of Erlebacher, Hussaini, Kreiss and Sarkar [7]. This field does not satisfy the Navier-Stokes equations, but

- its mean is aligned with x_1 and equals U_1;
- the spectrum of the fluctuation is defined by

$$E(k) = 16 \left(\frac{2}{\pi}\right)^{1/2} \frac{u_0^2}{k_0} \left(\frac{k}{k_0}\right)^4 \exp\left[-2\left(\frac{k}{k_0}\right)^2\right], \qquad (4)$$

  where $u_0 = 1$ is the rms value of any of the components of the fluctuation and $k_0 = 4$ the value of most energetic wave number (linked, for this spectrum, with the value of the Taylor microscale by $k_0 = 2/\lambda_0$);
- the fluctuating field ($\mathbf{u}$) is the sum of a divergence-free (rotational) field ($\mathbf{u}_s$) and a dilatational (irrotational) field ($\mathbf{u}_c$), the ratio (χ) of the dilatational to total turbulent kinetic energy being freely adjustable.

The random velocity field with constant pressure and density is used as an initial condition for the simulation of time-decreasing turbulence

in the cubic domain. Periodic boundary conditions are used in the three directions. Time-decay is stopped after the fluctuating fields are stabilized to a mean velocity derivative skewness ($S = (S_1 + S_2 + S_3)/3$, with $S_\alpha = \overline{(\partial u'_\alpha/\partial x_\alpha)^3}/[\overline{(\partial u'_\alpha/\partial x_\alpha)^2}]^{3/2}$) of -0.45 (at $t = 0.75\tau_t$, where $\tau_t = \lambda_0/u_0$) that makes them reasonably representative of real turbulence.

Input data for the interaction with the solenoidal and acoustic modes are generated with $\chi = 0$ and $\chi = 0.5$ respectively. Generating the input data for the entropy mode is slightly different. We begin with $\chi = 0$, constant pressure and density. As soon as the mean velocity-derivative skewness has reached the value -0.45 (at $t = 0.35\tau_t$), pressure fluctuations are set to zero while temperature and density fluctuations are specified according to:

$$\frac{\rho'}{\overline{\rho}} = -\frac{T'}{\overline{T}} = (\gamma - 1)\, M_1^2\, \frac{u'_1}{\overline{u}_1}, \tag{5}$$

which satisfies the Strong Reynolds Analogy (SRA). The calculation then proceeds until S reaches -0.45 again. Generally, a single turbulent field is not sufficient to perform the full simulation of the interaction. Additional instantaneous fields with the same statistical properties are derived analytically from the initial field using the procedure proposed by Mahesh *et al.* [31].

Table II summarizes the statistical properties of the incoming turbulence for the two values of the Mach number and the three modes. What really matters is the value of each of these parameters immediately before the shock, theses values are also reported in the table. One can easily check that, in the case of the solenoidal and acoustic modes, pressure and density fluctuations are nearly isentropic as reported by Kovasznay [23] ($p'_{\rm rms}/\overline{p} \approx \gamma\, \rho'_{\rm rms}/\overline{\rho}$); and that, in the case of the entropy mode, the Strong Reynolds Analogy holds ($\rho'_{\rm rms}/\overline{\rho} \approx T'_{\rm rms}/\overline{T} \approx$

$(\gamma - 1)M_1^2\, u'_{1\,\mathrm{rms}}/\overline{u}_1$ and $\overline{u'_1 T'} \approx -u'_{1\,\mathrm{rms}} T'_{\mathrm{rms}}$, which corresponds to a negative correlation between the longitudinal velocity and temperature fluctuations). Note also that in all cases, we have $M_t < 0.2$ and $M_t^2 < 0.1(M_1^2 - 1)$, so that the pressure fluctuations associated with the turbulent motion are small compared to the pressure jump across the shock. The linearization of the Rankine-Hugoniot relations performed in LIA is therefore fully justified (see Lee *et al.* [25]), allowing systematic comparison between the simulation and LIA results in the next section.

3. Results and discussion

From now on, we adopt the following convention to denote the different cases of interaction that have been computed: I1.5sol (resp. I1.2sol) refers to the interaction between the Mach-1.5 (resp. 1.2) shock and solenoidal turbulence; I1.5ent (resp. I1.2ent) to the interaction between the Mach-1.5 (resp. 1.2) shock and turbulence dominated by vorticity and entropy fluctuations; and I1.5ac (resp. I1.2ac) to the interaction between the Mach-1.5 (resp. 1.2) shock and turbulence dominated by vorticity and pressure fluctuations.

The simulation results are recorded when a statistically steady state is established in the computational domain (typically after one flow-through time). Turbulence statistics are then computed by averaging over the two homogeneous directions and time. We use 60 instantaneous fields saved during the simulation with a time sampling interval of $2\tau_t/60$ so that the size of the statistical sample is 60×128^2 and the total size of the time sample is $2\tau_t$. Apart from the conventional Reynolds average, we shall use Favre's mass-weighted average. For a

given function f, it is defined by $\tilde{f} = \overline{\rho f}/\overline{\rho}$, and the corresponding fluctuation is denoted by f''.

Linear analysis has been performed for all the cases of interaction with spectra of the form (4), where $u_0 = 1$ and $k_0 = 4$.

3.1. General characteristics of the interaction

The most important features of the interaction are examined with the simulation results obtained in the case I1.5sol. Most of these results have already been reported by previous authors with different flow parameters. We provide however in this section a summary of the main aspects of the problem based on our computations. This will be useful to the understanding of section 3.2. Comparisons between the main existing numerical and experimental data with linear analysis are also provided in order to sum up the state of the art in the field.

3.1.1. *Amplification of turbulence and generation of anisotropy*

The main consequences of the passage of a turbulent flow through a shock wave are the amplification of the fluctuating motion and generation of anisotropy. This is apparent in Figure 2 where the evolutions of Favre's Reynolds stresses $R_{ij} = \overline{\rho u_i'' u_j''}/\overline{\rho}$ across the shock have been plotted. The vertical dashed lines denote the limits of the mean shock zone, corresponding to the locations where $\partial \overline{u}_1/\partial x_1 = 0$. It can be seen that the transverse components (R_{22} and R_{33}) are amplified across the shock, while the streamwise Reynolds stress (R_{11}) experiences a non-monotonic behaviour: a slight reduction is observed immediately behind the shock (near-field), followed by a significant increase. Further away, all three Reynolds stresses undergo a consistent viscous decay; return to isotropy in this region is found to be negligible compared to

the decay rate. In the vicinity of the outflow, an unphysical rise of the streamwise Reynolds stress can be observed, the spurious dilatation levels generated by the non-reflective boundary conditions specified in this plane are responsible for this behaviour. However, different tests were conducted to check that these perturbations are confined in the vicinity of the exit plane and do not influence the interaction zone. Amplification factors for the Reynolds stresses can be evaluated as the ratios between the maximum values downstream – outside the mean shock zone – and the values taken immediately before. Our results for these ratios have been plotted in Figures 3a and 3b together with those obtained by different authors and our LIA results for the far field, in a range of Mach numbers comprised between 0 and 3. One can notice a good overall agreement between the different results – especially for the transverse Reynolds-stress –, even if a quantitative comparison remains delicate: LIA refers to an inviscid approach while the low Reynolds number of the simulations ($Re_\lambda = 6.7$ in our case) is responsible for non-negligible viscous effects. In particular, the maximum of the streamwise Reynolds stress behind the shock is obviously affected by the viscous decay and underestimated in the simulation (as compared to the inviscid analysis). This underestimation is mainly linked to the physical (natural) viscosity of the problem and is not significantly worsen by the intrinsic numerical damping of the numerical scheme. Indeed, in the present computations, the numerical viscosity can be considered small compared to the physical one which is itself quite high given the low Reynolds number of the DNS. At least two remarks may support this statement. First, it can be shown that a theoretical estimation of the shock thickness corresponds to the numerical prediction. In the theoretical estimation, this thickness is linked to the physical viscosity of the problem. In the computations, the shock

thickness is driven by the *effective* viscosity, *i.e.* the sum of the physical viscosity and the numerical one. Since the theoretical estimation of the shock thickness corresponds to the numerical prediction, we can conclude that the effective viscosity is close to the physical one, in other words, that the numerical viscosity is small. Second, it can be seen in the validations presented in the appendix that the spatial decay of isotropic turbulence at low Reynolds number is correctly predicted by the numerical scheme (see Figures 28 and 29, where a comparison with theory is presented). Since the turbulence decay is driven by viscosity, the agreement between numerical predictions and theory shows again that the effective viscosity is close to the physical one, and that the numerical viscosity has not a significant contribution. One should finally note that a better agreement with LIA for the amplification factor of R_{11} has been obtained by Lee *et al.* [27, 28], Mahesh *et al.* [32] and Garnier *et al.* [11] in simulations at higher microscale Reynolds number (≈ 20).

The mechanisms responsible for the amplification of turbulence and non-monotonic evolution of R_{11} can be identified by computing the different terms in the Reynolds-stress transport equations. Considering R_{11}, with the various hypothesis we made concerning the flow (stationarity, homogeneity in the transverse directions, zero-mean transverse velocity components), the budget equation can be written as follows:

$$\begin{aligned} \underbrace{\overline{\rho}\tilde{u}_1 \frac{\partial R_{11}/2}{\partial x_1}}_{(I)} &= \underbrace{-\overline{\rho} R_{11} \frac{\partial \tilde{u}_1}{\partial x_1}}_{(II)} \underbrace{- \overline{u_1''} \frac{\partial \overline{p}}{\partial x_1}}_{(III)} \\ &\underbrace{- \overline{u_1'' \frac{\partial p'}{\partial x_1}}}_{(IV)} \underbrace{- \frac{1}{2} \frac{\partial (\overline{\rho R_{11} u_1''})}{\partial x_1}}_{(V)} \underbrace{+ \overline{u_1'' \frac{\partial \tau_{1k}}{\partial x_k}}}_{(VI)}. \end{aligned} \tag{6}$$

The different terms in this budget are shown in Figure 4, where only the portion of the domain located in the vicinity of the shock is presented (*i.e.* $8 < k_0 x_1 < 20$). Outside the shock zone, advection (I) is balanced by viscous dissipation (VI). These are the only significant terms, except just behind the shock (*i.e.* $13.2 < k_0 x_1 < 18$) where the pressure-work term (IV) acts as a positive source in the R_{11} budget. This term is a sink in the R_{22} budget in the near-field and becomes quickly negligible (not shown here). Pressure work thus appears as responsible for the non-monotonic behaviour of the streamwise Reynolds stress (and hence of the turbulent kinetic energy) immediately downstream of the shock. More information can be obtained by decomposing the pressure-work term – as it appears in the transport equation of the Favre-averaged turbulent kinetic energy ($\tilde{k}$) – in two contributions as:

$$\underbrace{-\overline{u_i''\frac{\partial p'}{\partial x_i}}}_{\text{p. work}} = \underbrace{\overline{p'\frac{\partial u_i''}{\partial x_i}}}_{\text{p. dilatation}} \underbrace{-\frac{\partial(\overline{p'u_i''})}{\partial x_i}}_{\text{p. diffusion}} . \tag{7}$$

Figure 5 displays these terms. The positive pressure dilatation is responsible for an energy transfer from the mean internal energy to the turbulent kinetic energy immediately behind the shock. This production of $\tilde{k}$ is then transferred downstream *via* pressure diffusion which occurs only in the non-homogeneous direction. The non-monotonic evolution of R_{11} (and $\tilde{k}$) in the near-field is thus driven by the pressure-diffusion term.

Amplification of turbulence and generation of anisotropy can also be observed on the evolution of the fluctuating vorticity. Figure 6 shows the behaviour of the variances of the three components of fluctuating vorticity in the interaction. The transverse components ($\overline{\omega_2'^2}$ and $\overline{\omega_3'^2}$) appear to be significantly increased through the shock while the stream-

wise component ($\overline{\omega_1'^2}$) is barely affected. Note however that Lee *et al.* [27] showed an increase of $\overline{\omega_1'^2}$ behind the shock for higher values of the turbulent Reynolds number. Amplification factors can be evaluated in the same way as for the Reynolds stresses, they have been plotted in Figure 7 together with other simulation data and the LIA result. Here, the maxima occur immediately behind the shock and are therefore little affected by viscous decay. Consequently, the amplification factors are all in good agreement despite the low Reynolds numbers of the simulations, an exception is the results of Hannappel and Friedrich [13] which is significantly underpredicted.

The differences in the behaviour of the streamwise and transverse vorticity components can also be analysed using the budget equations of their variances under the form:

$$\begin{aligned}
\underbrace{\overline{u}_j \frac{\partial \overline{\omega'_\alpha \omega'_\alpha}}{\partial x_j}}_{(I)} \;=\; & \underbrace{2\,\overline{\omega'_\alpha \omega'_j}\,\overline{s}_{\alpha j}}_{(II)} \;\; \underbrace{+\,2\,\overline{\omega'_\alpha \omega'_j s'_{\alpha j}}}_{(III)} \\
& \underbrace{-\,2\,\overline{\omega'_\alpha \omega'_\alpha}\,\overline{s}_{jj}}_{(IV)} \;\; \underbrace{-\,\overline{\omega'_\alpha \omega'_\alpha s'_{jj}}}_{(V)} \\
& \underbrace{+\,2\epsilon_{\alpha jk}\,\overline{\frac{1}{\rho^2}\omega'_\alpha \frac{\partial \rho}{\partial x_j}\frac{\partial p}{\partial x_k}}}_{(VI)} \;\; \underbrace{-\,\frac{\partial(\overline{\omega'_\alpha \omega'_\alpha u'_k})}{\partial x_k}}_{(VII)} \\
& \underbrace{+\,2\epsilon_{\alpha jk}\,\overline{\omega'_\alpha \frac{\partial}{\partial x_j}\left(\frac{1}{\rho}\frac{\partial \tau_{kq}}{\partial x_q}\right)}}_{(VIII)},
\end{aligned} \tag{8}$$

where $s_{ij} = 1/2(\partial u_i/\partial x_j + \partial u_j/\partial x_i)$, and ϵ_{ijk} stands for the permutation tensor (no summation on α). One can see in Figure 8 that inside the shock region, compression by the mean flow (IV) is the dominant term for $\overline{\omega_2'^2}$, resulting in the observed amplification of the transverse

vorticity components. In the budget of $\overline{\omega_1'^2}$, this term is canceled by the mean vortex stretching (II), which leads to the absence of variation across the shock for this component of the vorticity fluctuation.

3.1.2. *Evolution of the turbulent length scales*

Modifications of the characteristic length scales of turbulence is an essential feature of the interaction that still remains a conflicting point in the literature: all the numerical studies indicate a global decrease of these scales in contradiction with most experiments except those by Barre *et al.* [1]. Further comments will be made on the subject in section 3.2.3. At this point, we simply provide in Figure 9 the reduction factor of the transverse Taylor microscale as obtained from our simulation and previous investigations. The Taylor microscale is defined as:

$$\lambda_\alpha = \left[\overline{u_\alpha'^2} \Big/ \overline{\left(\frac{\partial u_\alpha'}{\partial x_\alpha} \right)^2} \right]^{1/2}, \tag{9}$$

with $\alpha = 2$ for the transverse direction. Only DNS and LIA results are given in the figure since most of the experimental values are above unity. Moreover, we only consider the transverse microscale, since the longitudinal one evolves rapidly behind the shock wave (cf. Figure 18) so that a precise definition of the reduction factor is not easy. Comparison of the one-dimensional energy spectra of the velocity fluctuations before and after the shock (not shown here) is in agreement with Lee *et al.* [27], indicating that the reduction of the microscales during the interaction corresponds to an enhancement of the fluctuations at large wavenumbers.

3.1.3. *Amplification of the thermodynamic fluctuations*

Fluctuations in the thermodynamic quantities ($p'_{\rm rms}$, $\rho'_{\rm rms}$ and $T'_{\rm rms}$) are also enhanced through the shock. This amplification (see Figure 21) is followed by a rapid decay immediately behind the shock. An interesting topic to investigate is the thermodynamic state after the interaction. When thermodynamic fluctuations are isentropic, the following relation is satisfied:

$$\frac{p'}{\overline{p}} = n\frac{\rho'}{\overline{\rho}} = \frac{n}{n-1}\frac{T'}{\overline{T}}, \tag{10}$$

with $n = \gamma$. We can then define two coefficients $n_{p\rho}$ and $n_{\rho T}$ as:

$$n_{p\rho} = \frac{\sqrt{\overline{p'^2}}/\overline{p}}{\sqrt{\overline{\rho'^2}}/\overline{\rho}} \qquad \text{and} \qquad n_{\rho T} = 1 + \frac{\sqrt{\overline{T'^2}}/\overline{T}}{\sqrt{\overline{\rho'^2}}/\overline{\rho}}, \tag{11}$$

with $n_{p\rho} = n_{\rho T} = \gamma$ for isentropic fluctuations. When the incident turbulent flow only contains vorticity fluctuations, the isentropic hypothesis is satisfied upstream of the shock. We compare in Figure 10 the values obtained here for $n_{p\rho}$ and $n_{\rho T}$ downstream of the shock with those obtained in previous computations and LIA for solenoidal upstream turbulence. DNS and LIA are in close agreement: the isentropic state persists downstream only for weak shock waves ($M_1 < 1.2$), while the production of entropy fluctuations during the interaction increases with the value of the Mach number (see also Lee *et al.* [28]). This is an important point in turbulence modelling since two different polytropic exponents (instead of one) will be necessary to fully determine the thermodynamic state behind a strong shock wave.

3.2. Influence of the nature of the incoming turbulence

We shall now investigate how the behaviour of the main statistics of the flow across the shock wave are affected by the nature of the upstream turbulence. This point is addressed in this section for the three types of turbulence mentioned earlier. Compared to the existing contributions to the field, attention is given to perform the comparisons with the same parameters, the difference between the cases lying exclusively in the nature of the incident flow in term of Kovasznay's decomposition. New conclusions are also drawn from the simulation data completing the existing knowledge of the situation.

3.2.1. *Velocity fluctuations*

We present in Figure 11 the spatial evolutions of the normal Reynolds stresses R_{11} and R_{22} in the three computations at Mach 1.5 and 1.2. The corresponding results obtained with the linear analysis are given in Figure 12. One can notice a clear influence of the nature of the incident flow on the interaction, and a good agreement between DNS and LIA results. The presence of upstream entropy fluctuations satisfying SRA increases the level reached by the Reynolds stresses far behind the shock wave (mainly for the streamwise component) as compared to the reference case. The maximum levels reached for R_{11} behind the shock in DNS (at $k_0 x_1 = 16$) are 1.29 and 1.76 for cases I1.5sol and I1.5ent, respectively (difference of 36.6%). The corresponding values, predicted by LIA, are 1.59 and 2.54 (difference of 60.1%). Concerning R_{22}, the increase due to entropy fluctuations reaches 10.5% in DNS and 15.7% in LIA. A quantitative comparison between DNS and LIA seems difficult since the conditions are not exactly the same in both approaches: when entropy fluctuations are present, SRA holds exactly

in the analysis while it is approximately satisfied in DNS (see table II). Moreover, viscosity is still very important in the computations whereas it is not considered in LIA. When $M_1 = 1.2$, the same observations can be made even if the amplification of R_{11} is only 12.6% higher in case I1.2ent compared to I1.2sol (22.6% in LIA). Concerning R_{22}, the differences are small [cf. Figure 11b (down)]: 2.6% in DNS and 5.1% in LIA.

The presence of significant pressure fluctuations in the incoming turbulence seems to slightly reduce the far-field level of the diagonal Reynolds-stress-tensor components. Moreover, small perturbations appear for the different statistics of the flow near the inflow plane in cases I1.5ac and I1.2ac. These perturbations contrast with the regular behaviour obtained in the other computations. They are due to the forcing used at the entrance of the domain where the solenoidal and dilatational parts of the velocity field are advected at the same speed, which should not be the case in real life. Turbulence therefore rapidly adjusts near the inflow boundary. The amplification of R_{11} is 6% lower in the case I1.5ac compared to I1.5sol (for $k_0 x_1 = 16$). The corresponding reduction in LIA amounts to 39% at the same location. R_{22} is unaffected in the computations while a 43.3% difference is predicted by the linear theory. The I1.5ac simulation corresponds to an incident flow containing pressure and vorticity fluctuations while the corresponding case in the analysis deals with a pure acoustic turbulent flow upstream of the shock. Thus, comparison between DNS and LIA is not satisfactory in this situation and a ponderation of LIA results needs to be made to account for the fact that the incoming turbulence is not purely acoustic in the simulation (cf. Mahesh *et al.* [30]). If acoustic and vorticity fluctuations are combined in the analysis, linearity allows the amplification factor of the kinetic energy being written in the following

way:

$$\frac{q_2^2}{q_1^2} = \frac{(q_2^2)_S + (q_2^2)_C}{(q_1^2)_S + (q_1^2)_C}, \tag{12}$$

where subscripts '1' and '2' refers to upstream and downstream values, with 'S' and 'C' representing the solenoidal and dilatational components respectively. Equation (12) may then be reformulated, introducing the ratio of compressible to total upstream kinetic energy $\chi = (q_1)_C^2/q_1^2$, as:

$$\frac{q_2^2}{q_1^2} = (1-\chi)\frac{(q_2^2)_S}{(q_1^2)_S} + \chi\frac{(q_2^2)_C}{(q_1^2)_C}. \tag{13}$$

The combined problem may thus be treated from the amplification factors obtained for q^2 in the pure vortical and the pure acoustic limits. Applying Equation (13) to R_{11} and R_{22} with $\chi = 0.5$ leads to an amplification factor of 1.28 for R_{11} and 1.08 for R_{22}. The reductions of 39% and 43.3% mentioned before, become 19.3% and 21.4%, respectively, in the combined problem. The comparison between DNS and LIA is thus better, even if some discrepancies still exist. The observed reduction of the amplification factor of the Reynolds stresses by upstream pressure fluctuations should however happen mainly in the range $1.25 < M_1 < 1.8$, as predicted by LIA in Figure 13. One can see that the amplification factor of the kinetic energy is less than 1 only in that range of Mach numbers. This is confirmed by the results of the computations at $M_1 = 1.2$, where no noticeable difference appears in the evolutions of R_{11} and R_{22} between the cases I1.2sol and I1.2ac.

3.2.2. *Vorticity fluctuations*

We now investigate the influence of the different modes of turbulence on the vorticity variances across the shock. No major difference between the three cases appears for the streamwise component $\overline{\omega_1'^2}$, while the

amplification of $\overline{\omega_2'^2}$ is seen to increase by 19.3% in the case I1.5ent compared to I1.5sol [see Figure 14a(down)]. This is once again in good qualitative agreement with LIA which predicts no amplification of $\overline{\omega_1'^2}$ in all cases and an increase of 31.5% in the amplification factor of $\overline{\omega_2'^2}$ when upstream entropy fluctuations satisfying SRA are present (the solenoidal case is still the reference). The corresponding values, when $M_1 = 1.2$, are 7.5% [DNS – see Figure 14b(down)] and 20% (LIA). As mentioned in the introduction, Mahesh *et al.* [32] proposed an explanation based on the relative effects of bulk compression and baroclinic torque to understand the influence of entropy fluctuations. This explanation relied on physical considerations and linear analysis. We show here that their interpretation is confirmed by our DNS results. As a matter of fact, in both cases (see Figures 15a and 15b for I1.5sol and I1.5ent respectively), the budgets of the transverse vorticity show that bulk compression is responsible for the amplification of $\overline{\omega_2'^2}$. Moreover, the relative importance of bulk compression is the same in both simulations. However, in the vorticity-entropy case, the compression by the mean flow is not the only positive contribution inside the shock and the baroclinic torque also plays an important role. Figure 16 compares the importance of this term in the budgets of the transverse vorticity for the three simulations. It is clear that, in the I1.5ent case, the baroclinic torque is not negligible, in contradiction with what is observed in the other configurations. In order to quantify when entropy fluctuations play a role, the ratio of the rms entropy fluctuation to the mean upstream entropy ($s'_{\rm rms}/\overline{S}_1$) has been computed for the different cases (see table II). One can see that in the I1.2ent and I1.5ent cases, this ratio amounts to 1% and 1.26% respectively just before the shock wave, whereas it is well below this value in the other computations. A

threshold value around 1% for this criterion thus seems to be adequate to indicate if the entropy fluctuation level is high enough upstream of the shock wave to influence the interaction.

When pressure fluctuations are present upstream of the shock at $M_1 = 1.5$ (I1.5ac), the amplification of $\overline{\omega_2'^2}$ is also greater than in the case I1.5sol, but the difference is far less important than before. No difference is observed when $M_1 = 1.2$. Hannappel and Friedrich [13] already mentioned the same kind of behaviour even if the difference between the solenoidal and the 'compressible' cases was more important in the simulations they conducted for a Mach 2 shock wave. An explanation for the preceding observations may be provided using LIA. We present in Figure 17 the far-field amplification ratio of the turbulent kinetic energy as a function of the upstream Mach number obtained in the pure acoustic case. The vortical and dilatational contributions of the kinetic energy are also displayed. It is clear that, when $M_1 \leq 1.5$, too few vorticity is generated during the interaction to make a difference in the amplification of $\overline{\omega_2'^2}$. The contribution of the vortical part of the kinetic energy becomes however more significant when $M_1 = 2$.

3.2.3. *Turbulent length scales*

As we shall see, the qualitative behaviour of the different turbulent scales across the shock is globally independent of the nature of the upstream turbulent flow. However, the downstream level is not the same in the different computations.

The spatial evolutions of the longitudinal and transversal microscales are displayed in Figure 18 for the computations at Mach 1.5. No noticeable difference appears between the three cases for λ_1, while λ_2 is more reduced in the case I1.5ent: the difference amounts to 3% between I1.5sol and I1.5ent. For $M_1 = 1.2$, this value falls to 1.2%. These

trends agree with LIA results since the analysis predicts no difference in the behaviour of λ_1 across the shock, between the solenoidal and vorticity/entropy cases. Concerning λ_2, LIA predicts a 5% (resp. 3%) larger reduction when the upstream turbulence contains entropy fluctuations at Mach 1.5 (resp. 1.2). When upstream pressure fluctuations are present, λ_1 is still unaffected and λ_2 is less reduced than in the solenoidal case. The difference amounts to 11% for $M_1 = 1.5$ and 6% for $M_1 = 1.2$. These results confirm Hannappel and Friedrich's conclusion of a reduction in the transverse microscale 50% less important in the compressible case ($\chi = 0.5$) than in the solenoidal case ($\chi = 0$) for $M_1 = 2$.

Figure 19 displays the spatial evolution of the transverse integral scales of the flow defined as:

$$\Lambda_{ii,\alpha} = \int_0^\infty Q_{ii,\alpha}(r)\ dr, \tag{14}$$

where the auto-correlation of the velocity component u_i' in the x_α-direction is obtained from the following expression:

$$Q_{ii,\alpha}(r) = \frac{\overline{u_i'(\mathbf{x})u_i'(\mathbf{x}+r\mathbf{e}_\alpha)}}{\overline{u_i'(\mathbf{x})u_i'(\mathbf{x})}}.$$

We observe a significant reduction of $\Lambda_{11,2}$ and $\Lambda_{22,2}$ across the shock. This reduction of $\Lambda_{11,2}$ (resp. $\Lambda_{22,2}$) is 28% (resp. 14%) higher in the vorticity/entropy case.

An increase of the 'dissipation' length scale $l_\varepsilon = \overline{\rho} q^3/\varepsilon \sim \tilde{k}^{3/2}/\varepsilon$ is also apparent in Figure 20. This is in agreement with the LIA results of Lee *et al.* [28] according to which l_ε should increase for Mach numbers less than 1.65 and decrease above, simulation results by the same authors confirmed this point. One should note however the reported amplification of l_ε at Mach 2 by Hannappel and Friedrich, which is

in contradiction with Lee's conclusions. Another interesting point may be emphasized concerning the behaviour of this turbulent scale: for solenoidal turbulence, l_ε is assumed to be representative of the largest scales of the fluctuating motion (l), and the following relation holds: $l \sim l_\varepsilon \sim \Lambda_{11,2}$. This property is widely used in turbulence modelling through Batchelor's hypothesis [2]: $\varepsilon \sim \tilde{k}^{3/2}/l_\varepsilon \sim \tilde{k}^{3/2}/\Lambda_{11,2}$. However, in the present computation, l_ε and $\Lambda_{11,2}$ behave in a radically different way. The classic estimation of Batchelor should consequently not be used if turbulence models are applied to shock-turbulence interaction situations. Moreover, one can notice that the amplification factor of the dissipation scale is not significantly affected by the nature of the upstream turbulence. However, the rapid increase of l_ε just behind the shock is more pronounced when upstream entropy fluctuations are present. This is an indirect manifestation of the behaviour reported earlier for the turbulent velocity fluctuations.

All the preceding features concerning turbulent scales are in agreement with LIA. However, the discrepancies that still exist between DNS and experimental studies remain difficult to explain. Many parameters may influence the behaviour of the turbulence statistics across the shock, like for instance shock strength (M_1), turbulent Mach number (M_t) or microscale Reynolds number (Re_λ). Since these parameters are very different between most of the experimental and numerical works (Briassulis and Andreopoulos [3] considered Reynolds numbers between 162 and 737 and Honkan and Andreopoulos [16] worked with $Re_\lambda \sim 1000$, whereas $Re_\lambda < 30$ in all the computations), this may be one of the reason to this problem. This interpretation is coherent with the fact that, in the experiment by Barre *et al.* [1] at $Re_\lambda = 15.5$, the behaviour of the integral scales across the shock is in qualitative agreement with DNS and LIA.

3.2.4. *Thermodynamic quantities*

As shown in Figure 21, the presence of upstream entropy fluctuations leads to a higher amplification of $p'_{\rm rms}$ across the shock compared to the solenoidal case, whereas the opposite is true for $\rho'_{\rm rms}$ and $T'_{\rm rms}$. Moreover, when pressure fluctuations are associated to the rotational mode in the incident turbulent flow, the amplification of all the thermodynamic quantities is lower than in the solenoidal case. Hannappel and Friedrich [13] reported the same behaviour in their computations at $M_1 = 2$.

We already mentioned in Section 3.1 that for solenoidal upstream turbulence, thermodynamic fluctuations remain isentropic downstream only if $M_1 \leq 1.2$. For higher Mach numbers, the production of entropy fluctuations during the interaction leads to a deviation from the isentropic state downstream of the shock. When the acoustic and vortical modes are associated upstream, the isentropic state persists for $M_1 = 1.5$ everywhere in the computational domain since the relation $p'_{\rm rms}/\overline{p} = \gamma\rho'_{\rm rms}/\overline{\rho} = \gamma T'_{\rm rms}/(\gamma-1)\overline{T}$ holds on both sides of the shock (see Figure 22).

In the vorticity/entropy cases, the upstream thermodynamic fluctuations are obviously not isentropic since SRA holds approximately. It is then interesting to test the validity of this hypothesis downstream of the shock wave. The different terms of Equation (5) are shown in Figures 23a and 23b for cases I1.5ent and I1.2ent respectively. In each configuration, comparison is made with linear analysis and a very good qualitative agreement is displayed between both approaches, particularly when $M_1 = 1.5$. In this case, the intensity of pressure fluctuations is comparable to the other quantities in the near-field and becomes lower in the far-field. Strong deviation from SRA appears in the near-field, while in the far-field, the first part of relation (5) relating density

and temperature fluctuations is satisfied but not the second part of the equation concerning velocity fluctuations. Besides, the deviation is more important in the linear analysis than in the DNS where viscous effects rapidly damp the gap between the different terms. All these results agree with the observations made by Mahesh *et al.* [32] for $M_1 = 1.29$ and $M_1 = 1.8$.

4. Summary and conclusion

Numerical simulation of the interaction between shock waves at Mach number 1.2 and 1.5 and three types of isotropic turbulence has been performed. A numerical code based on a standard second-order-accurate numerical scheme was used and care was taken to warrant a complete resolution of the shock wave as well as adequate resolution of the turbulent fields.

The general characteristics of the interaction have been investigated in the case of a solenoidal upstream turbulent field and are in fair agreement with most existing simulations, theoretical and experimental results. Comparisons between the existing contributions have been provided. Evaluation of the different terms in the Reynolds-stress budget equations helps to draw a detailed picture of the mechanisms that lead to the amplification of the turbulent kinetic energy across the shock, and a difference in the behaviour of the transverse and streamwise Reynolds stresses. As in previous numerical studies, and still in contradiction with most experiments, our results exhibit a decrease in the turbulent length scale when turbulence passes through the shock. The reason for this discrepancy remains unclear and should be further investigated.

The interactions with three different types of incoming turbulence for each value of the upstream Mach number have then been computed. The first type is purely solenoidal, the second contains vorticity and entropy fluctuations (satisfying the Strong Reynolds Analogy) and the last type is mainly composed of vorticity and pressure fluctuations. Our results confirm earlier findings obtained by different authors with different flow conditions. The downstream levels of the main statistics have been shown to depend on the kind of turbulence which is introduced in the computational domain. The presence of upstream entropy fluctuations enhances the amplification of the turbulent kinetic energy and transverse vorticity variances across the shock compared to the solenoidal case. More reduction of the transverse Taylor microscale and integral scale is observed in the vorticity-entropy case while no influence can be seen on the longitudinal Taylor microscale. When acoustic and vortical fluctuations are associated upstream, less amplification of the kinetic energy, less reduction of the transverse microscale and more amplification of the transverse vorticity variance are observed across the shock.

New conclusions have also been drawn from the data obtained. Fluctuating vorticity budgets have been computed and show that the baroclinic torque is responsible for the additional production of transverse vorticity in the vorticity/entropy case, in agreement with an interpretation based on linear analysis given by Mahesh *et al.* [32]. Moreover, the classic estimation of Batchelor relating the dissipation rate and the integral scale of the flow was seen to be invalid for the modelisation of shock/turbulence interaction situations. LIA was also conducted in the same interaction cases and proved to be in good agreement with the simulation results. Thanks to the theory, the influence of the acoustic mode on the amplification of the kinetic energy has been

shown to be noticeable only for Mach numbers comprised between 1.25 and 1.8.

The description of the different mechanisms involved in the interaction will be helpful to understand more complicated phenomena like for instance the interaction between a shock and a supersonic boundary layer. In this situation, SRA is satisfied and the presence of entropy fluctuations should strongly promote the amplification of turbulence as reported in this work. The different conclusions of the preceding analysis should also be useful for the development of more accurate compressible turbulence models. Free turbulence-shock interaction is an idealized situation that allows the influence of the compressible terms in the budgets of the different statistics of the turbulent flow being reliably evaluated. It thus appears as a good candidate to elaborate and test closure schemes for these terms.

Acknowledgements

This work was supported by the French Ministry of Defense.

Appendix

Due to its moderate order of accuracy, the ability of the code to resolve shock-turbulence interaction problems needs to be demonstrated. In a first step, we concentrate on temporal and spatial simulations of isotropic, decaying turbulence. Then, a more interesting situation is to consider the two-dimensional interaction between a shock and a plane

vorticity-entropy wave since it allows a direct comparison with LIA results.

Temporal simulations of isotropic, decaying turbulence.

We first checked the behaviour of the code regarding turbulence: temporal and spatial simulations of isotropic, decaying turbulence without shock were thus conducted. The computational domain is a cube with dimensions of 2π in each direction. For temporal simulations, periodic boundary conditions are applied in all three directions. As stated in Section 2.3, the initialization of the flow results from the superposition of a random velocity field generated with the algorithm of Erlebacher *et al.* [7] on the following mean field:

$$\overline{u}_1 = U_1, \quad \overline{u}_2 = \overline{u}_3 = 0, \quad \overline{p} = \frac{1}{\gamma M_r^2}, \quad \overline{\rho} = 1. \tag{15}$$

In the simulations presented hereafter: $\chi = 0$ (solenoidal initial turbulence). The remaining parameters are the following: $Re_r = 13.4$, $M_r = 0.1$, $Pr = 0.7$, $M_1 = 1.5$, $u_0 = 1$, $k_0 = 4$. They are associated to a microscale Reynolds number $Re_\lambda = 6.7$, which corresponds to a resolution of 128^3. The turbulent Mach number is $M_t = q/\overline{c} = (\overline{u_i' u_i'})^{1/2}/\overline{c} = \sqrt{3}u_0/\overline{c} = 0.173$. A correct behaviour of the three-dimensional velocity spectra, turbulent length scales, microscale Reynolds number and velocity derivative skewness has been observed (not shown here). Moreover, three different grids (64^3, 128^3 and 192^3) were used with the same parameters to check adequate resolution of the turbulent flow. This evaluation was made through the one-dimensional velocity spectra defined as: $E_\alpha(k_2) = \overline{\hat{u}_\alpha(k_2)\hat{u}_\alpha^\star(k_2)}$, where $\hat{(\cdot)}$ stands for the Fourier transform along x_2 and $\overline{(\cdot)}$ denotes spatial averaging along x_1 and x_2. For incompressible isotropic turbulence, the following analytical

relation is satisfied (see Hinze [14]):

$$E_1(k_2) = E_3(k_2) = \frac{1}{2}\left[E_2(k_2) - k_2 \frac{\partial E_2(k_2)}{\partial k_2} \right]. \qquad (16)$$

These spectra are presented in Figure 24 for the three cases at the same time ($t/\tau_t = 0.75$, where $\tau_t = \lambda_0/u_0$ is a turbulence time scale). A lack of resolution can be observed for the highest wavenumbers with the 64^3 grid, while Equation (16) is correctly satisfied in the two other configurations. The 128^3 grid is therefore well suited for respectable DNS of turbulence at $Re_\lambda = 6.7$ with our second-order code. Grid independence of the main statistics of the flow is also apparent in Figures 25 and 26: no difference can be seen on the evolutions of the turbulent kinetic energy $q^2/2$ and the dissipation rate $\tilde{\varepsilon}$ of the flow between the different cases.

Spatial simulations of isotropic, decaying turbulence.

Proper simulation of spatially evolving turbulence is then the next step before considering shock-turbulence interaction cases. In this configuration, the inhomogeneity of the flow in the streamwise direction is the main difficulty to overcome. In this direction, turbulent fluctuations are prescribed as inflow conditions using Taylor's hypothesis, and all variables are specified since the flow is supersonic. These data correspond to several turbulent fields obtained from preliminary temporal simulations of the decay of solenoidal isotropic turbulence (see Section 2.3). They are superposed to the mean incoming flow (see Equation (15)) and updated at each time step. The outflow is supersonic and no boundary condition needs to be specified in the exit plane. The computational domain is still a cubic geometry of $(2\pi)^3$ with a regular grid of 128^3 points. The parameters of the simulation are the same as in the tem-

poral cases: $Re_r = 13.4$, $M_r = 0.1$, $Pr = 0.7$, $M_1 = 1.5$, $Re_\lambda = 6.7$, $M_t = 0.173$.

Figure 27 compares the evolutions of the longitudinal (S_1) and mean velocity derivative skewness $S = (S_1 + S_2 + S_3)/3$ in the temporal and spatial simulations conducted with the same parameters (with $S_\alpha = \overline{(\partial u'_\alpha/\partial x_\alpha)^3}/[\overline{(\partial u'_\alpha/\partial x_\alpha)^2}]^{3/2}$). Figures 28 and 29 present the same comparisons for the kinetic energy and the dissipation rate. The longitudinal and mean skewness factors reach a value of -0.4 in both cases, which is characteristic of a well-developed isotropic turbulent field (Orszag and Patterson [34]; Tavouralis, Bennet and Corrsin [39]). This value is obtained after a short transition period in the temporal simulation corresponding to the time necessary for the artificial initial conditions to become stationary solution of the Navier-Stokes equations. In the spatial case, inflow turbulent data come from already developed turbulent fields so that a much smaller transition period is observed (for S_1 only). Good agreement between the two simulations can also be noted on the evolutions of kinetic energy and dissipation. For these statistics, comparison with theory is possible owing to the following classical model of isotropic, decaying turbulence:

$$\begin{aligned} \frac{d\tilde{k}}{dt} &= -\frac{\tilde{\varepsilon}}{Re_r}, \\ \frac{d\tilde{\varepsilon}}{dt} &= -\frac{C_{\varepsilon_2}}{Re_r}\frac{\tilde{\varepsilon}^2}{\tilde{k}}, \end{aligned} \tag{17}$$

where $\tilde{k} = q^2/2$ and C_{ε_2} is the usual modelling constant. Solution of Equations (17) leads to the following analytical expressions:

$$\begin{aligned} \frac{\tilde{k}}{\tilde{k}_0} &= \left[1 + \frac{\tilde{\varepsilon}_0}{Re_r\tilde{k}_0}(C_{\varepsilon_2} - 1)t\right]^{\frac{1}{1-C_{\varepsilon_2}}}, \\ \frac{\tilde{\varepsilon}}{\tilde{\varepsilon}_0} &= \left[1 + \frac{\tilde{\varepsilon}_0}{Re_r\tilde{k}_0}(C_{\varepsilon_2} - 1)t\right]^{\frac{C_{\varepsilon_2}}{1-C_{\varepsilon_2}}}, \end{aligned} \tag{18}$$

with $\tilde{k}_0 = 1.5$ and $\tilde{\varepsilon}_0 = 60$. Perfect agreement between theory and the spatial simulation is displayed in Figures 28 and 29 when $C_{\varepsilon_2} = 1.5$. This value is slightly different from the standard 1.92 (Launder and Sharma [24]), however, Hanjalić and Launder [12] mentioned that C_{ε_2} should be a function of $R_T \equiv k^2/\nu\varepsilon$ according to: $C_{\varepsilon_2} = 1.8\ [1 - 0.4/1.8\ e^{-\left(\frac{1}{6}R_T\right)^2}]$. This expression gives values between 1.8 and 1.4 for C_{ε_2}, the latter corresponding to low Reynolds numbers. Two-point correlations $Q_{ii,\alpha}(r) = \overline{u_i'(\mathbf{x})u_i'(\mathbf{x}+r\mathbf{e}_\alpha)}/\overline{u_i'(\mathbf{x})u_i'(\mathbf{x})}$ and one-dimensional power spectra $E_\alpha(k_2)$ of the velocity field are finally plotted in Figures 30 and 31. The size of the computational domain as well as the resolution are seen to be adequate.

Vorticity-entropy wave/shock interaction.

An interesting elementary case of shock-turbulence interaction is now described. This test consists of a two-dimensional interaction between a plane vorticity-entropy wave and a Mach 1.5 shock wave. The parameters of the computations are still: $Re_r = 13.4$, $M_r = 0.1$ and $Pr = 0.7$. The computational domain has dimensions of 2π in both directions. A non-uniform grid that clusters points near the shock is used in the streamwise direction (x_1) while a uniform mesh of 32 points is used in the transverse direction (x_2). The flow is initialized with a steady normal shock wave (obtained with a preliminary calculation) over which the fluctuating vorticity-entropy wave is superposed at $t = 0$:

$$\begin{cases} u_1' = U_1 A_v \sin\psi_1 \cos(k_x x + k_y y) \\ v_1' = -U_1 A_v \cos\psi_1 \cos(k_x x + k_y y) \\ \rho_1' = \overline{\rho}_1 A_e \cos(k_x x + k_y y) \\ p_1' = 0 \end{cases} \tag{19}$$

where the subscript '1' refers to upstream values and the overbars denote mean quantities. The wavenumbers k_x and k_y are given by:

$$k_x = k\cos\psi_1, \qquad k_y = k\sin\psi_1,$$

where k is the magnitude of the wavenumber vector and ψ_1 denotes the angle between the wavenumber vector and x_1. The variables A_v and A_e correspond to the intensity of velocity and density upstream of the shock wave. They were both equal to 0.025. Periodic boundary conditions are specified in the transverse direction and non-reflecting boundary conditions are used at the outflow in the streamwise direction. At the inflow ($x_1 = 0$), an unsteady wave is superposed to the mean flow. This wave takes the following form:

$$\begin{cases} u_1' = U_1 A_v \sin\psi_1 \cos(k_y y - U_1 k_x t) \\ v_1' = -U_1 A_v \cos\psi_1 \cos(k_y y - U_1 k_x t) \\ \rho_1' = \overline{\rho}_1 A_e \cos(k_y y - U_1 k_x t) \\ p_1' = 0 \end{cases} \tag{20}$$

Several values for ψ_1 are considered inside the interval $[0; \pi/2]$. For each case, the wavenumber k is chosen so that we have one wavelength in the x_2 direction:

$$k_y = k\sin\psi_1 = 1, \qquad k_x = 1/\tan\psi_1.$$

The statistics of the flow are gathered after one flow-through time in order to let the initial transient exit the domain and cover one period of the incident disturbance. The behaviour of the code during the interaction is evaluated by comparing the values obtained for the amplification of vorticity fluctuations ($\overline{\omega_2'^2}/\overline{\omega_1'^2}$) to the linear analysis results. Figure 32 shows the comparison for two cases: the first one corresponds to a solenoidal incident wave ($A_e = 0,\ A_v = 2.5\%$) and the

second one to a vorticity-entropy wave ($A_e = A_v = 2.5\%$). Excellent agreement between computation and analysis is seen away from the critical angle $\psi_c = 61.36^{\circ}$: the difference between the two approaches never exceeds 5%. When ψ_1 comes close to ψ_c, Mahesh *et al.* [31] showed that LIA may be questionable: the deviation around the critical angle is thus a limitation of the linear analysis, not of the computation. The same test was also conducted for $M_1 = 1.2$, and the agreement between DNS and LIA was found even better than what has been shown here.

Considering the good results of all the different test cases, it can be concluded that reliable DNS of shock-turbulence interaction is possible using the second-order-accurate numerical scheme of MacCormack. This numerical method is however limited to moderate upstream Mach numbers and small microscale Reynolds numbers as shown by the grid resolutions needed in this work.

References

1. Barre, S., Alem, D. and Bonnet, J.-P., Experimental study of a normal shock/homogeneous turbulence interaction. *AIAA J.* **34** (1996) 968–974.
2. Batchelor, G.K., *The Theory of homogeneous turbulence.* Cambridge University Press, Cambridge (1953).
3. Briassulis, G. and Andreopoulos , J., High resolution measurements of isotropic turbulence interacting with shock waves. AIAA Paper 96-0042 (1996).
4. Debiève, J.-F. and Lacharme, J.-P., A shock wave/free turbulence interaction. In *Turbulent Shear Layer/Shock Wave Interactions*, edited by J. Delery, Springer (1985).
5. Dubois, T., Domaradzki, J.A. and Honein, A., The subgrid-scale estimation model applied to large eddy simulations of compressible turbulence. *Phys. Fluids A* **14**(5) (2002) 1781–1801.

6. Ducros, F., Ferrand, V., Nicoud, F., Weber, C., Darracq, D., Gacherieu C. and Poinsot, T., Large-eddy simulation of the shock/turbulence interaction. *J. Comp. Phys.* **152** (1999) 517–549.
7. Erlebacher, G., Hussaini, M.Y., Kreiss, H.O. and Sarkar, S., The analysis and simulation of compressible turbulence. *Theoret. and Comput. Fluid Dynamics* **2** (1990) 73–95.
8. Fabre, D., Jacquin, L., Garnier, E. and Sagaut, P., Linear interaction analysis: the effect of a shock wave on a homogeneous perturbation field and on an entropy spot. In *Turbulence in high speed compressible flows*, Euromech 403, Poitiers (1999).
9. Fabre, D., Jacquin, L. and Sesterhenn, J., Linear interaction of a cylindrical entropy spot with a shock. *Phys. Fluids A* **13**(8) (2001) 2403–2422.
10. Garnier, E., Sagaut, P. and Deville, M., A class of explicit ENO filters with application to unsteady flows. *J. Comp. Phys.* **170**(1) (2001) 184–204.
11. Garnier, E., Sagaut, P. and Deville, M., Large eddy simulation of shock/homogeneous turbulence interaction. *Computers and Fluids* **31**(2) (2002) 245–268.
12. Hanjalić, K. and Launder, B.E., Contribution towards a Reynolds-stress closure for low-Reynolds-number turbulence. *J. Fluid Mech.* **4** (1976) 593–610.
13. Hannappel, R. and Friedrich, R., Direct numerical simulation of a Mach 2 shock interacting with isotropic turbulence. *Appl. Sci. Res.* **54** (1995) 205–221.
14. Hinze, J., *Turbulence.* MacGraw-Hill, New York (1975).
15. Honkan, A. and Andreopoulos, J., Experiments in a shock wave/homogeneous turbulence interaction. AIAA Paper 90-1647 (1990).
16. Honkan, A. and Andreopoulos, J., Rapid compression of grid-generated turbulence by a moving shock wave. *Phys. Fluids A* **4** (1992) 2562–2572.
17. Honkan, A., Watkins, C.B. and Andreopoulos, J., Experimental study of interactions of shock wave with free-stream turbulence. *J. of Fluids Engineering* **116** (1994) 763–769.
18. Jacquin, L., Blin, E. and Geffroy, P., Experiments on free turbulence/shock wave interaction. *Proceedings of the eighth Symposium on Turbulent Shear Flows*, edited by F. Durst, R. Friedrich, B.E. Launder, F.W. Schmidt, U. Schumann and J.H. Whitelaw, Springer-Verlag, Munich, (1991).

19. Jacquin, L., Cambon C. and Blin, E., Turbulence amplification by a shock wave and rapid distortion theory. *Phys. Fluids A* **5**(10) (1993) 2539–2550.
20. Jacquin, L. and Geffroy, P., Amplification and reduction of turbulence in a heated jet/shock interaction. *Proceedings of the eleventh Symposium on Turbulent Shear Flows*, edited by F. Durst, B.E. Launder, F.W. Schmidt and J.H. Whitelaw, Springer-Verlag, Grenoble (1997).
21. Jamme, S., Étude de l'interaction entre une turbulence homogène isotrope et une onde de choc. PhD. Thesis, Institut National Polytechnique de Toulouse (1998).
22. Keller, J. and Merzkirch, W., Interaction of a normal shock wave with a compressible turbulent flow. *Experiments in Fluids* **8** (1990) 241–248.
23. Kovasznay, L.S.G., Turbulence in supersonic flow. *J. of the Aero. Sci.* **20** (1953) 657–682.
24. Launder, B.E. and Sharma, B.I., Application of the energy-dissipation model of turbulence to the calculation of flow near a spinning disc. *Letters in Heat and Mass Transfer* **1** (1974) 131–138.
25. Lee, S., Lele, S.K. and Moin, P., Interaction of isotropic turbulence with a shock wave. Report TF-52, Thermosciences Division, Mechanical Engineering Department, Stanford University (1992).
26. Lee, S., Lele, S.K. and Moin, P., Simulation of spatially evolving turbulence and the applicability of Taylor's hypothesis in compressible flow. *Phys. Fluids A* **4** (1992) 1521–1530.
27. Lee, S., Lele, S.K. and Moin, P., Direct numerical simulation of isotropic turbulence interacting with a weak shock wave. *J. Fluid Mech.* **251** (1993) 533–562.
28. Lee, S., Lele, S.K. and Moin, P., Interaction of isotropic turbulence with shock waves: effect of shock strength. *J. Fluid Mech.* **340** (1997) 225–247.
29. MacCormack, R.W., The effect of viscosity on hypervelocity impact cratering. AIAA Paper 69-354 (1969).
30. Mahesh, K., Lee, S., Lele, S.K. and Moin, P., The interaction of an isotropic field of acoustic waves with a shock wave. *J. Fluid Mech.* **300** (1995) 383–407.
31. Mahesh, K., Moin, P. and Lele, S.K., The interaction of a shock wave with a turbulent shear flow. Report TF-69, Thermosciences Division, Mechanical Engineering Department, Stanford University (1996).

32. Mahesh, K., Lele, S.K. and Moin, P., The influence of entropy fluctuations on the interaction of turbulence with a shock wave. *J. Fluid Mech.* **334** (1997) 353–379.
33. Moore, F.K., Unsteady oblique interaction of a shock wave with a plane disturbance. NACA TN 2879 (1953).
34. Orszag, S.A. and Patterson, G.S., Numerical simulation of three-dimensional homogeneous isotropic turbulence. *Phys. Review Letters* **28** (1972) 76–79.
35. Ribner, H.S., Convection of a pattern of vorticity through a shock wave. NACA TN 2864 (1953).
36. Ribner, H.S., Shock/turbulence interaction and the generation of noise. NACA TN 3255 (1954).
37. Ribner, H.S., Spectra of noise and amplified turbulence emanating from shock/turbulence interaction. *AIAA J.* **35** (1987) 436–442.
38. Rotman, D., Shock wave effects on a turbulent flow. *Phys. Fluids A* **3** (1991) 1792–1806.
39. Tavouralis, S., Bennet, J.C. and Corrsin, S., Velocity derivative skewness in small Reynolds number, nearly isotropic turbulence. *J. Fluid Mech.* **176** (1978) 63–69.
40. Thompson, K.W., Time dependent boundary conditions for hyperbolic systems I. *J. Comp. Phys.* **68** (1987) 1–24.
41. Thompson, K.W., Time dependent boundary conditions for hyperbolic systems II. *J. Comp. Phys.* **89** (1990) 439–461.

Table I. Summary of the main parameters used in the different works on shock/turbulence interaction. For experimental works, Re_M stands for a Reynolds number based on the mesh size of the turbulence grid. The nature of the upstream turbulent flow (dominant modes) are only conjectured in the experiments. "sol, ent, ac" are abbreviations for solenoidal, entropic and acoustic modes respectively.

DNS				
	M_1	M_t	Re_λ	upstream turbulence
Rotman [38]	1.34	n.r.	n.r.	sol
Lee [27]	1.05-1.2	0.0567-0.11	11.9-21.6	sol
Lee [28]	1.5 ; 2 ; 3	0.0897-0.11	15.7-19.7	sol
Mahesh [32]	1.29 ; 1.8	0.14	19.1-19.5	sol/ent
Hannappel [13]	2	0.1	5-6.7	sol/ac
Present work	1.2 ; 1.5	0.173	5-6.7	sol/ent/ac
LES				
Ducros [6]	1.2	0.075	n.r.	sol
Garnier [11]	1.2 ; 2	0.136 ; 0.108	11.9 ; 19	sol
Dubois [5]	1.29	0.137-0.152	17.29-33.2	sol
Experiments (wind tunnels)				
	M_1	M_t	Re_M	Re_λ	upstream turbulence
Debiève [4]	2.3	n.r.	n.r.	n.r.	sol/ac
Jacquin [18]	1.4	≈ 0.05	97215	122.8	sol/ac
Jacquin [20]	1.6	≈ 0.07-0.123	n.r.	n.r.	sol/ent
Barre [1]	3	≈ 0.011	57301	15.5	sol/ac
Experiments (shock tubes)					
	1.115		35000		
Keller [22]	1.18	n.r.	58000	n.r.	sol/ac
	1.22		74000		
Honkan [15]	1.62	≈ 0.05	30480	≈ 1000	sol/ac
Honkan [16]	1.62	≈ 0.033	30480	≈ 1000	sol/ac
Honkan [17]	1.62	≈ 0.04	30480	≈ 1000	sol/ac
Briassulis [3]	1.551-2.183	≈ 0.02-0.06	37138-577040	162-735	sol/ac

Table II. Turbulence features in the inflow plane and immediately before the shock (between brackets) for the different simulations performed.

	I1.5sol	I1.5ent	I1.5ac	I1.2sol	I1.2ent	I1.2ac
$Re_\lambda = Re_r \frac{u'_{1\,\mathrm{rms}}\lambda}{\overline{\nu}}$	6.7	6.7	5	6.7	6.7	5
	(5.5)	(5.6)	(5.3)	(5.1)	(5.15)	(5.15)
$Re_t = Re_r \frac{u'_{1\,\mathrm{rms}}\Lambda}{\overline{\nu}}$	21	21	21	21	21	21
	(16.1)	(16.2)	(17.5)	(15.6)	(15.7)	(16.9)
$M_t = \frac{q}{\overline{c}}$	0.173	0.173	0.173	0.173	0.173	0.173
	(0.133)	(0.134)	(0.134)	(0.127)	(0.128)	(0.126)
$q^2/2$	1.5	1.5	1.5	1.5	1.5	1.5
	(0.89)	(0.9)	(0.89)	(0.81)	(0.82)	(0.8)
S	-0.45	-0.43	-0.46	-0.45	-0.43	-0.46
	(-0.43)	(-0.43)	(-0.44)	(-0.43)	(-0.43)	(-0.36)
$u'_{1\,\mathrm{rms}}/U_1$	0.067	0.067	0.067	0.083	0.083	0.083
	(0.051)	(0.051)	(0.055)	(0.061)	(0.061)	(0.066)
$p'_{\mathrm{rms}}/\overline{p}$	0.021	0.026	0.146	0.022	0.026	0.143
	(0.019)	(0.019)	(0.089)	(0.025)	(0.026)	(0.08)
$\rho'_{\mathrm{rms}}/\overline{\rho}$	0.017	0.058	0.103	0.017	0.048	0.102
	(0.014)	(0.041)	(0.064)	(0.012)	(0.031)	(0.057)
$T'_{\mathrm{rms}}/\overline{T}$	0.006	0.056	0.042	0.006	0.045	0.041
	(0.0057)	(0.04)	(0.025)	(0.021)	(0.036)	(0.03)
$(\gamma-1)M_1^2 u'_{1\,\mathrm{rms}}/U_1$	0.06	0.06	0.06	0.048	0.048	0.048
	(0.046)	(0.046)	(0.049)	(0.035)	(0.035)	(0.038)
$\overline{u'_1 T'}/u'_{1\,\mathrm{rms}} T'_{\mathrm{rms}}$	0.008	-0.91	-0.02	0.012	-0.91	-0.021
	(0.295)	(-0.86)	(0.393)	(0.257)	(-0.8)	(0.372)
$s'_{\mathrm{rms}}/\overline{S}_1$	0.001	0.0182	0.0014	0.0027	0.0149	0.0029
	(0.0009)	(0.0126)	(0.0011)	(0.0026)	(0.01)	(0.0028)

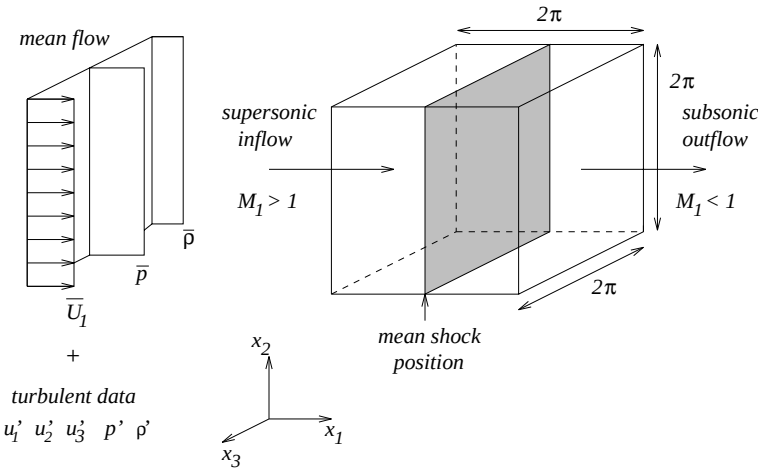

Figure 1. Schematic representation of the flow configuration.

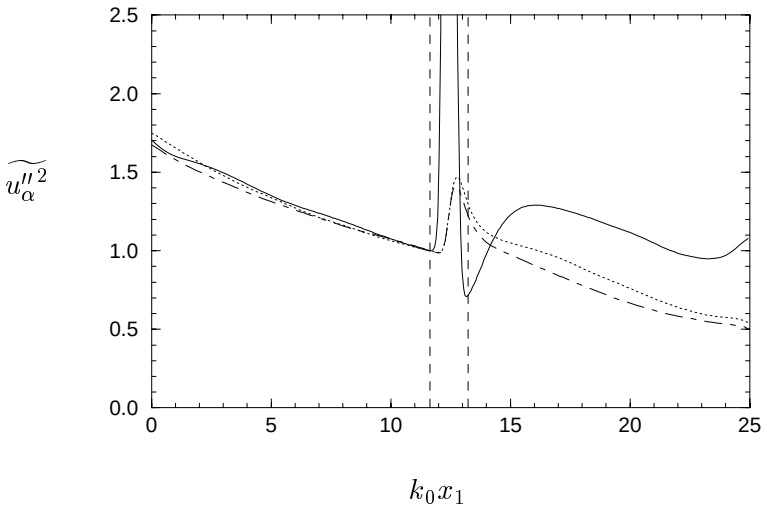

Figure 2. Evolution of the normal components of the Reynolds-stress tensor throughout the computational domain - DNS, I1.5sol. All the curves are normalized by the value immediately upstream of the shock. (——) $\widetilde{u_1''^2}$; (· · · · ·) $\widetilde{u_2''^2}$; (— · —) $\widetilde{u_3''^2}$.

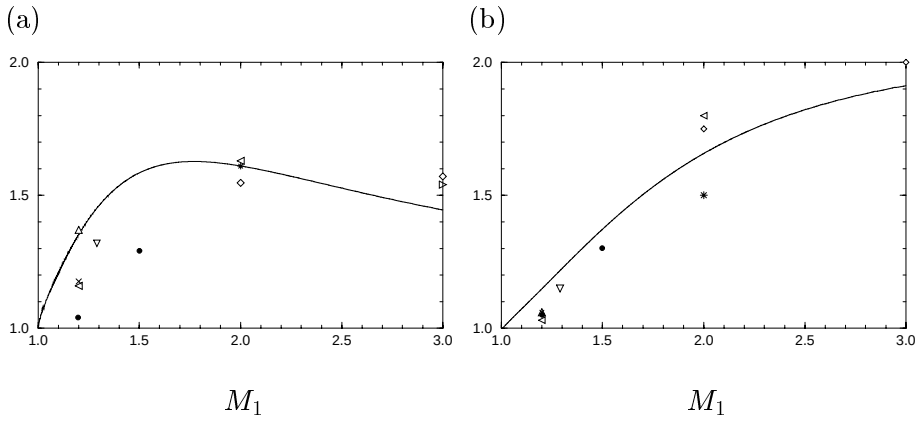

Figure 3. Amplification factor of the streamwise [R_{11}-(a)] and transverse [R_{22}-(b)] Reynolds-stress components across the shock wave. (——) LIA; (•) Present work; (×) Lee *et al.* [27]; (◇) Lee *et al.* [28]; (▽) Mahesh *et al.* [32]; (∗) Hannappel & Friedrich [13]; (△) Ducros *et al.* [6]; (◁) Garnier *et al.* [11]; (▷) Barre *et al.* [1].

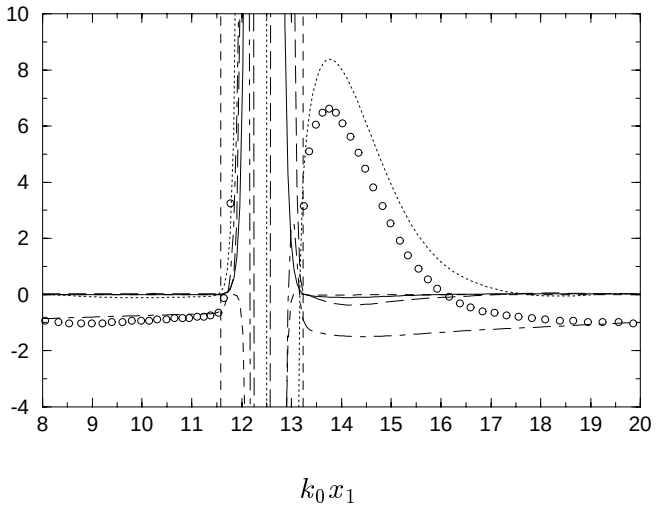

Figure 4. Different terms in the budget equation for R_{11} - DNS, I1.5sol. (∘ ∘ ∘) advection (I); (——) production by the mean strain (II); (– – –) production by the mass-flux fluctuations (III); (·····) pressure work (IV); (— —) turbulent diffusion (V); (– · –) viscous dissipation (VI).

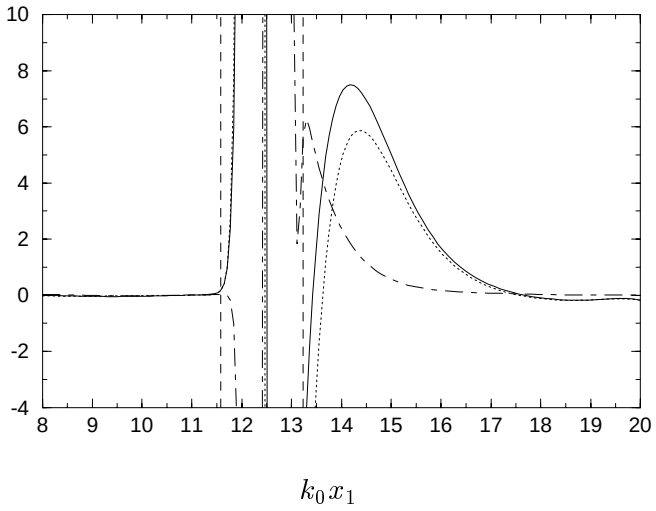

Figure 5. Pressure work decomposition in the budget equation for $\tilde{k}$ - DNS, I1.5sol. (——) $-\overline{u_i'' \dfrac{\partial p'}{\partial x_i}}$; (· · · · ·) $-\dfrac{\partial(\overline{p' u_i''})}{\partial x_i}$; (– · –) $\overline{p' \dfrac{\partial u_i''}{\partial x_i}}$.

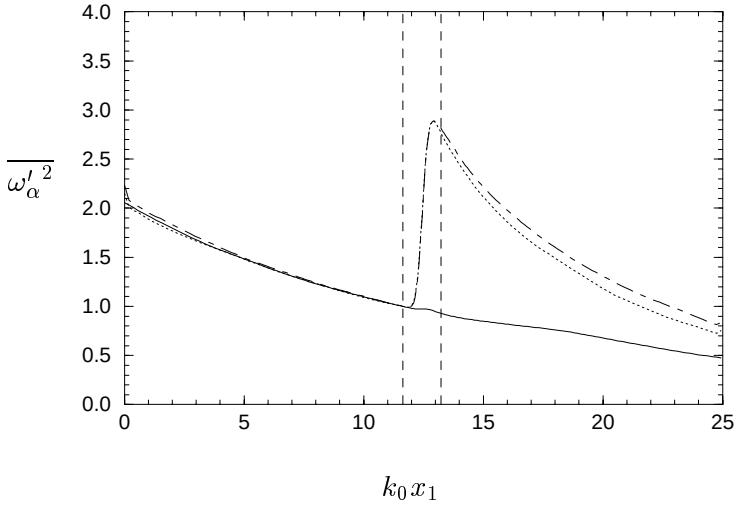

Figure 6. Evolution of vorticity fluctuations variances throughout the computational domain - DNS, I1.5sol. All the curves are normalized by the value immediately upstream of the shock. (——) $\overline{\omega_1'^{\,2}}$; (· · · · ·) $\overline{\omega_2'^{\,2}}$; (– · –) $\overline{\omega_3'^{\,2}}$.

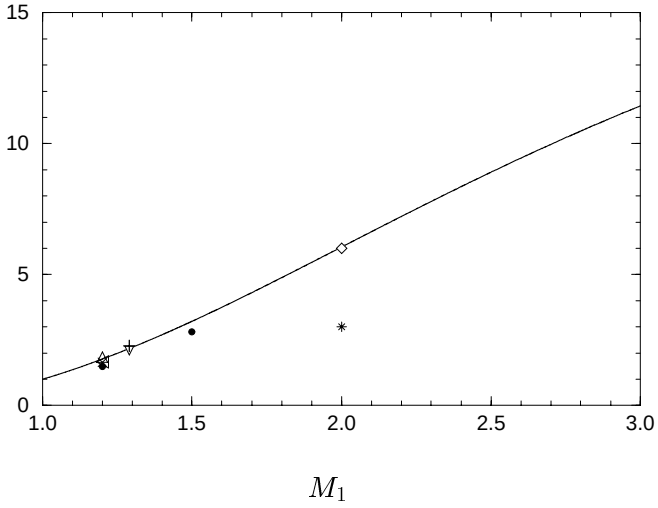

Figure 7. Amplification factor of the transverse vorticity variance $\overline{\omega_2'^2}$ across the shock wave. (——) LIA; (•) Present work; (×) Lee *et al.* [27]; (◇) Lee *et al.* [28]; (▽) Mahesh *et al.* [32]; (∗) Hannappel & Friedrich [13]; (△) Ducros *et al.* [6]; (◁) Garnier *et al.* [11]; (+) Dubois *et al.* [5].

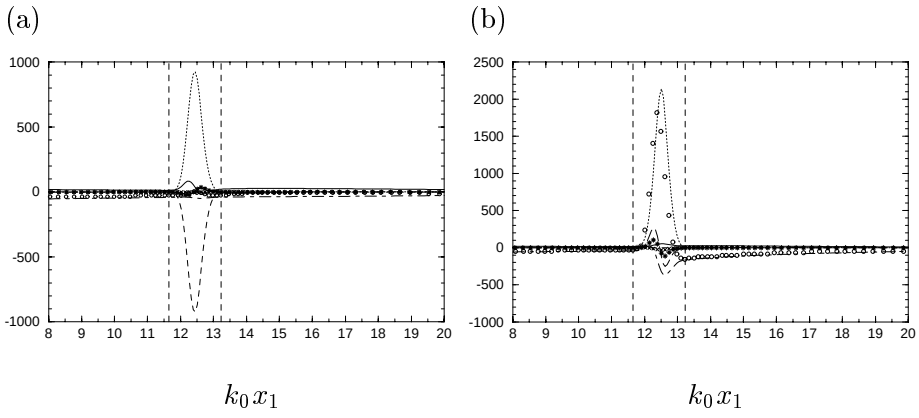

Figure 8. Different terms in the $\overline{\omega_1'^2}$ (a) and $\overline{\omega_2'^2}$ (b) budget equations - DNS, I1.5sol. (∘ ∘ ∘) advection (I); (– – –) stretching by the mean flow (II); (——) stretching by turbulence (III); (· · · · ·) compression by the mean flow (IV); (∗ ∗ ∗) compression by turbulence (V); (× × ×) baroclinic torque (VI); (— —) turbulent diffusion (VII); (– · –) viscous terms (VIII).

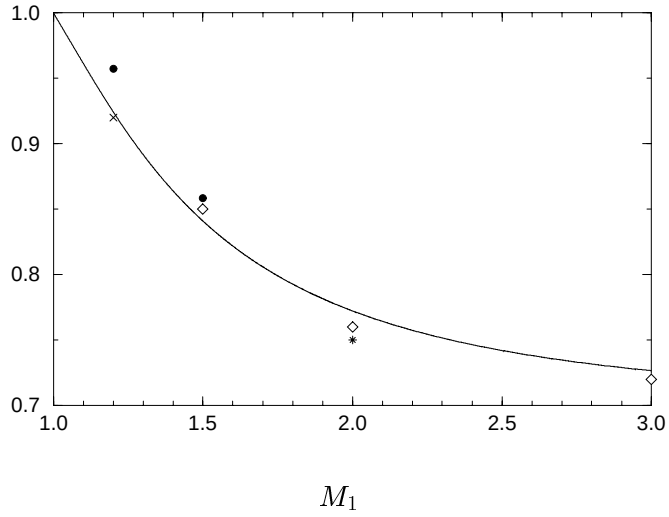

Figure 9. Change of the transverse Taylor microscale λ_2 across the shock wave. (——) LIA; (•) Present work; (×) Lee *et al.* [27]; (◇) Lee *et al.* [28]; (∗) Hannappel & Friedrich [13].

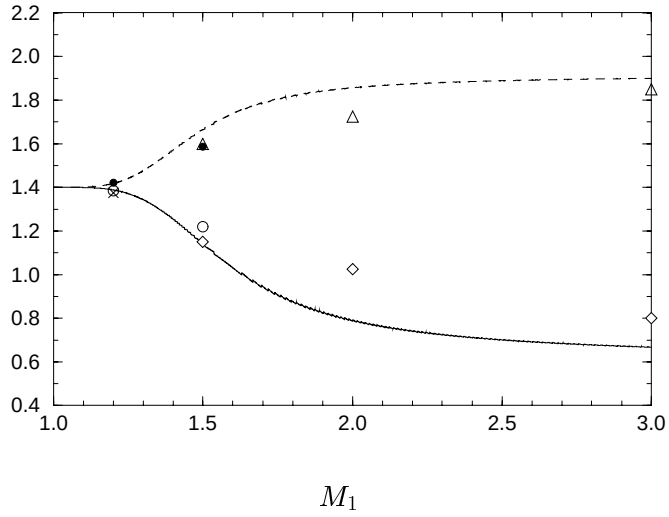

Figure 10. Downstream value of the polytropic exponents. (——) $n_{p\rho}$ LIA; (– – –) $n_{\rho T}$ LIA; (•) $n_{p\rho}$ present work; (○) $n_{\rho T}$ present work; (×) $n_{p\rho}$ Lee *et al.* [27]; (◇) $n_{p\rho}$ Lee *et al.* [28]; (△) $n_{\rho T}$ Lee *et al.* [28].

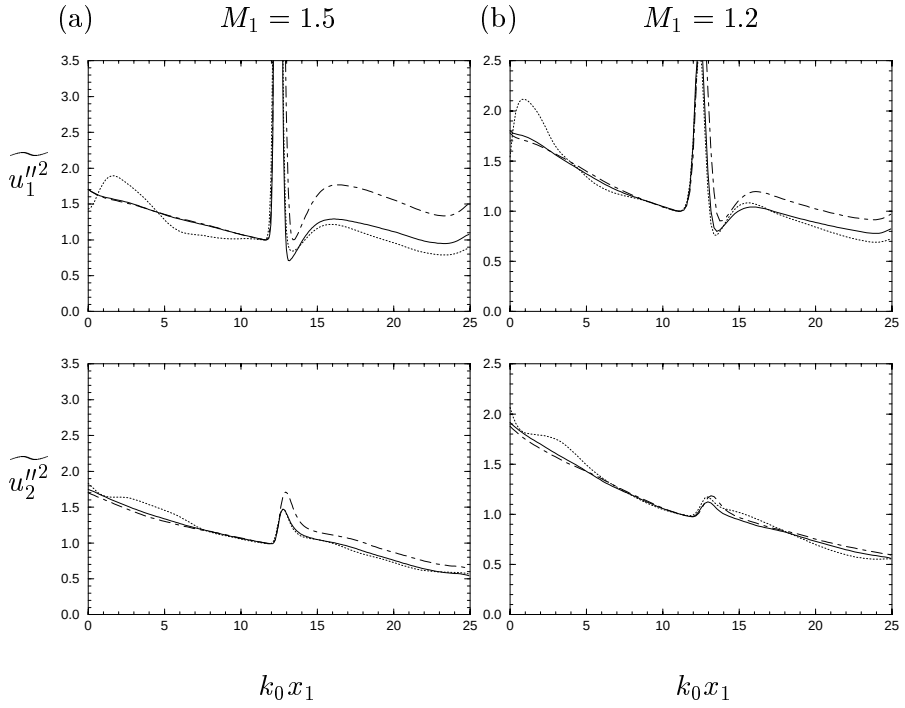

Figure 11. Influence of the different modes of turbulence on the evolutions of R_{11} (up) and R_{22} (down) across the shock wave - DNS, $M_1 = 1.5$ (a) and $M_1 = 1.2$ (b). All the curves are normalized by the value immediately upstream of the shock. (——) I1.5sol (a) or I1.2sol (b), (– · –) I1.5ent (a) or I1.2ent (b), (· · · · ·) I1.5ac (a) or I1.2ac (b).

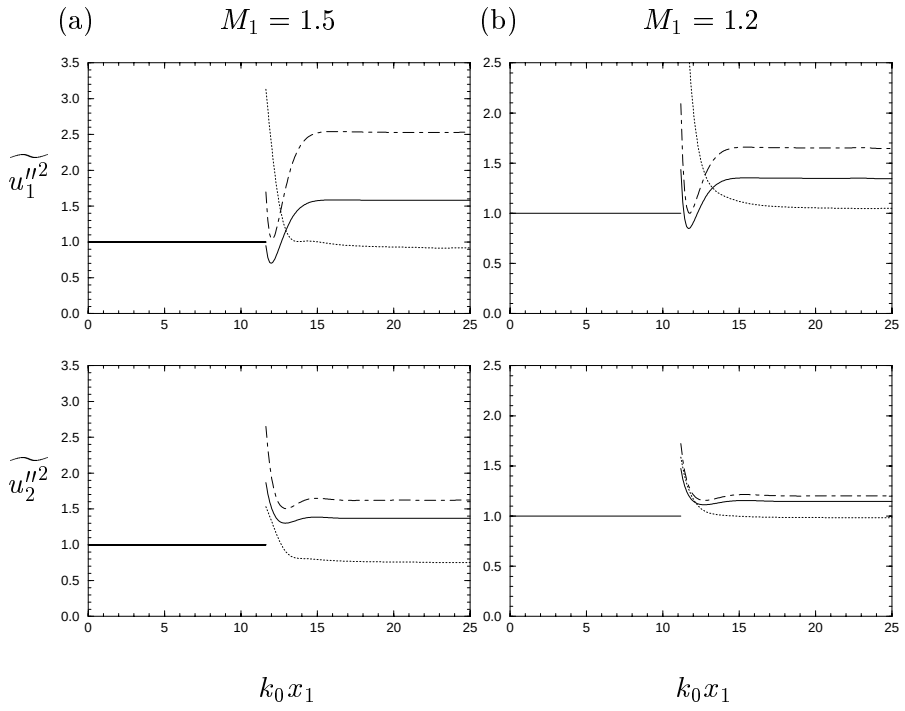

Figure 12. Influence of the different modes of turbulence on the evolutions of R_{11} (up) and R_{22} (down) across the shock wave - LIA, $M_1 = 1.5$ (a) and $M_1 = 1.2$ (b). All the curves are normalized by the value immediately upstream of the shock. (——) pure vorticity case, (– · –) vorticity/entropy case, (· · · · ·) pure acoustic case.

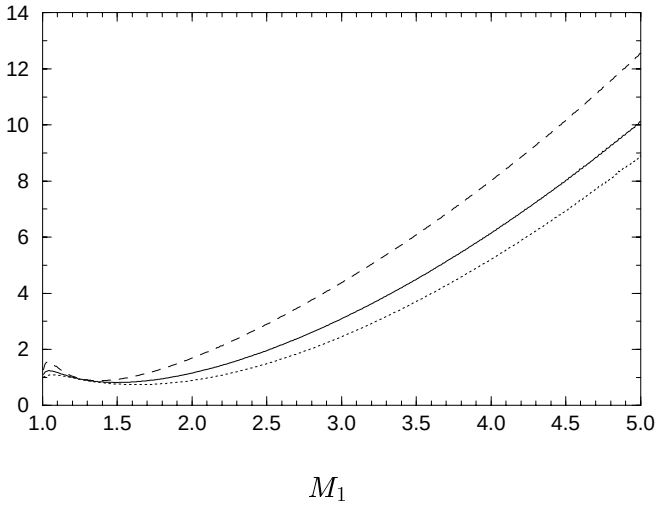

Figure 13. Far-field amplification factor of the velocity variances as predicted by linear analysis in the pure acoustic case. (——) q_2^2/q_1^2; (− − −) $\overline{u_2'^2}/\overline{u_1'^2}$; (· · · · ·) $\overline{v_2'^2}/\overline{v_1'^2}$.

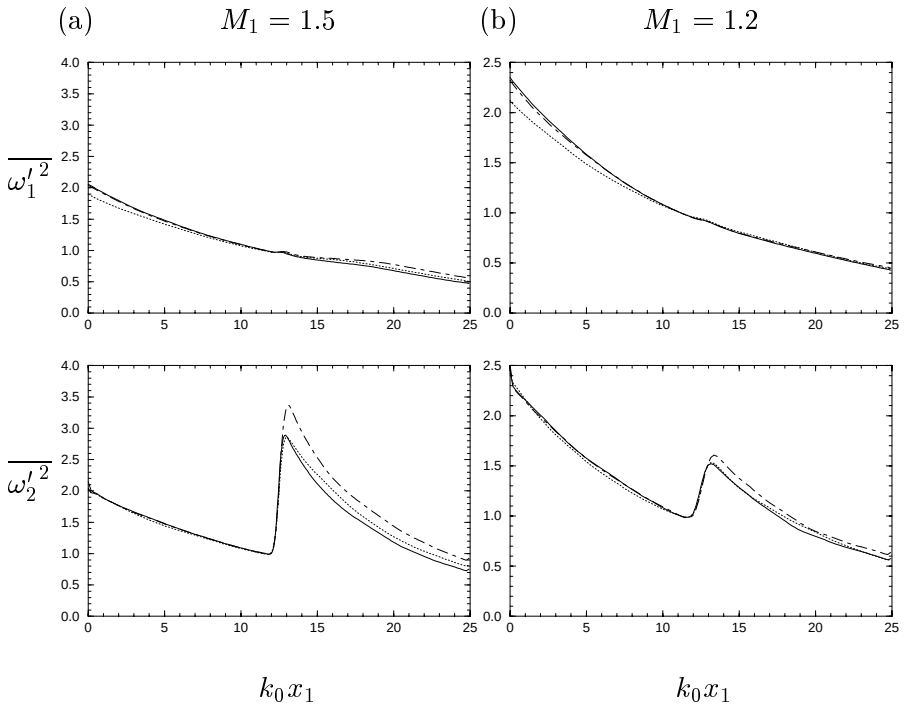

Figure 14. Influence of the different modes of turbulence on the evolutions of $\overline{\omega_1'^2}$ (up) and $\overline{\omega_2'^2}$ (down) across the shock wave - DNS, $M_1 = 1.5$ (a) and $M_1 = 1.2$ (b). All the curves are normalized by the value immediately upstream of the shock. (——) I1.5sol (a) or I1.2sol (b), (– · –) I1.5ent (a) or I1.2ent (b), (· · · · ·) I1.5ac (a) or I1.2ac (b).

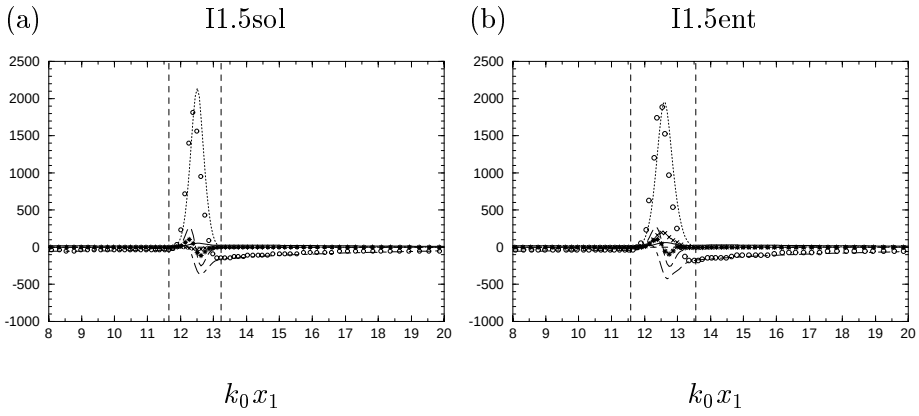

Figure 15. Different terms in the $\overline{\omega_2'^2}$ budget equations - DNS, I1.5sol (a) and I1.5ent (b). (ooo) advection (I); (– – –) stretching by the mean flow (II); (——) stretching by turbulence (III); (· · · · ·) compression by the mean flow (IV); (∗ ∗ ∗) compression by turbulence (V); (× × ×) baroclinic torque (VI); (— —) turbulent diffusion (VII); (– · –) viscous terms (VIII).

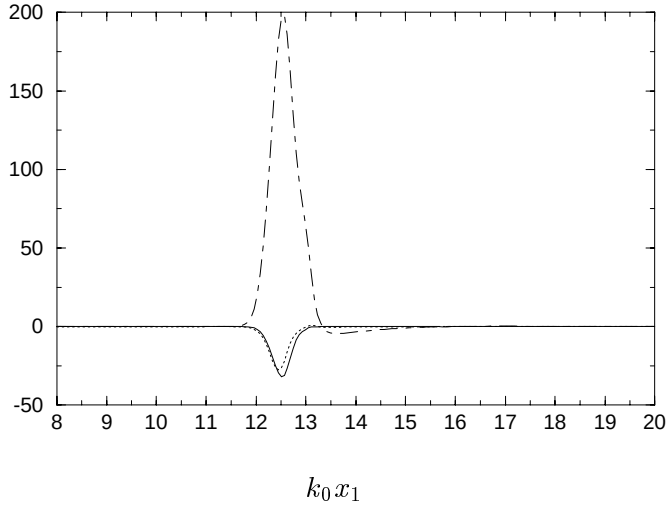

Figure 16. Comparison of the baroclinic torque in the budget equations for $\overline{\omega_2'^2}$. (——) I1.5sol, (– · –) I1.5ent, (· · · · ·) I1.5ac.

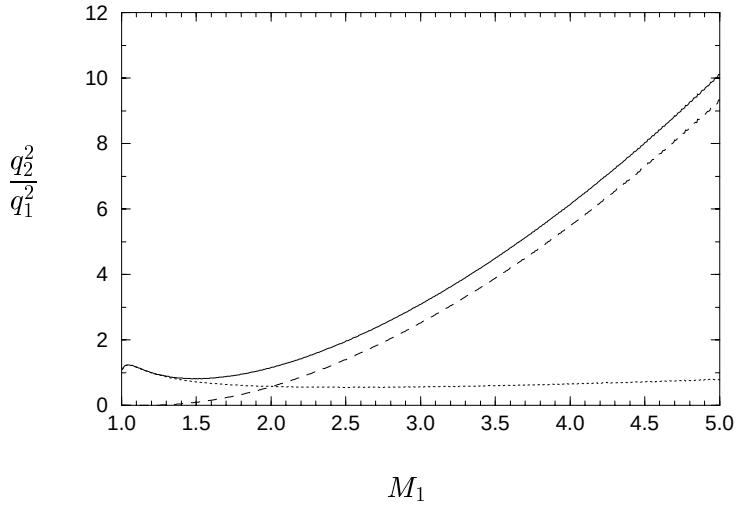

Figure 17. Far-field amplification ratio of the kinetic energy obtained in LIA for a pure acoustic incident turbulence. (——) total kinetic energy; (– – –) vortical component; (· · · · ·) acoustic component.

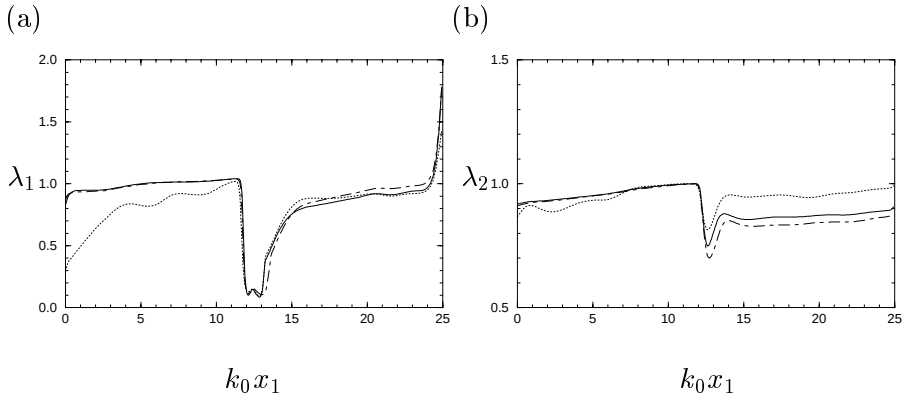

Figure 18. Influence of the different modes of turbulence on the evolutions of λ_1 (a) and λ_2 (b) across the shock wave - DNS, $M_1 = 1.5$. All the curves are normalized by the value immediately upstream of the shock. (——) I1.5sol, (– · –) I1.5ent, (· · · · ·) I1.5ac.

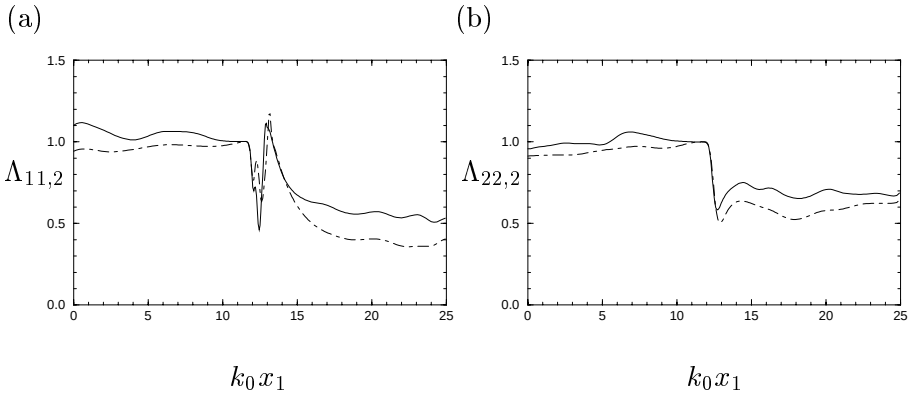

Figure 19. Influence of entropy fluctuations on the evolutions of $\Lambda_{11,2}$ (a) and $\Lambda_{22,2}$ (b) across the shock wave - DNS, $M_1 = 1.5$. All the curves are normalized by the value immediately upstream of the shock. (——) I1.5sol, (– · –) I1.5ent.

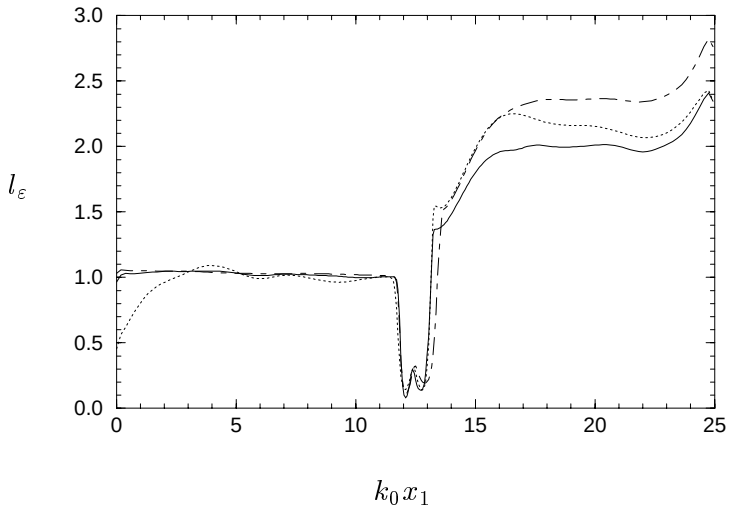

Figure 20. Influence of the different modes of turbulence on the evolutions of l_ε across the shock wave - DNS, $M_1 = 1.5$. All the curves are normalized by the value immediately upstream of the shock. (——) I1.5sol, (– · –) I1.5ent, (· · · · ·) I1.5ac.

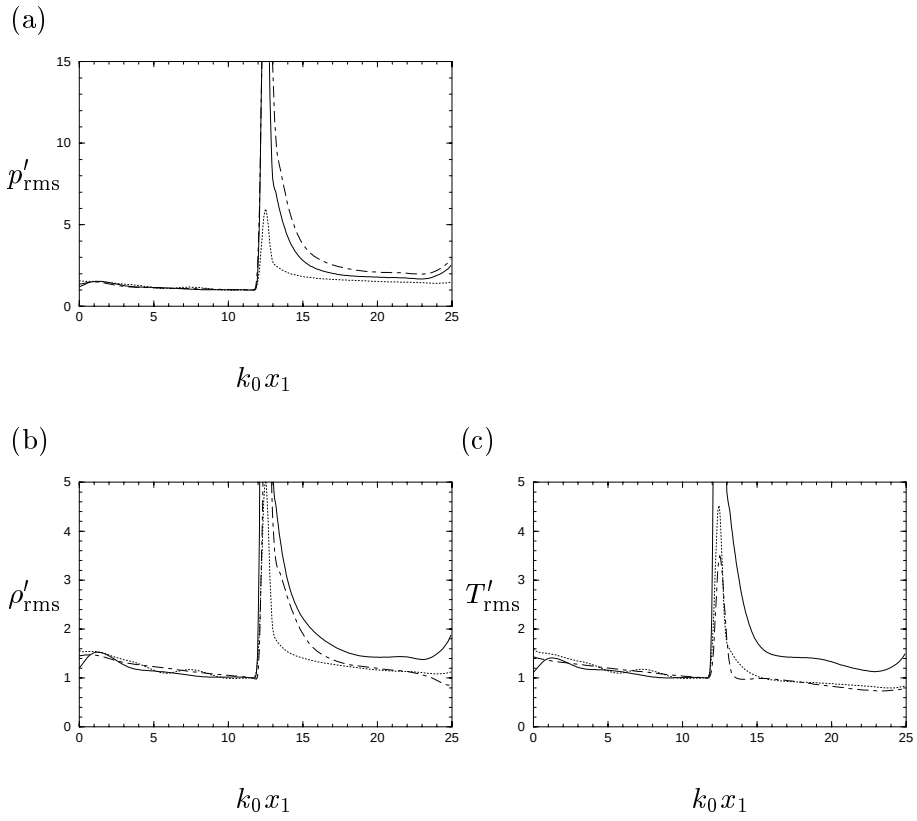

Figure 21. Influence of the different modes of turbulence on the evolutions of p'_{rms} (a), ρ'_{rms} (b) and T'_{rms} (c) across the shock wave - DNS, $M_1 = 1.5$. All the curves are normalized by the value immediately upstream of the shock. (——) I1.5sol, (– · –) I1.5ent, (· · · · ·) I1.5ac.

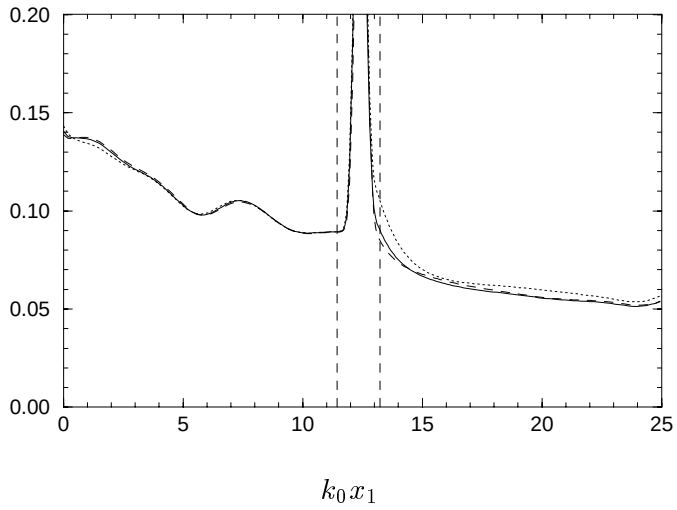

Figure 22. Evolution of rms values of the thermodynamic properties throughout the computational domain - DNS, I1.5ac. (——) $p'_{\rm rms}/\overline{p}$; (− − −) $\gamma\rho'_{\rm rms}/\overline{\rho}$; (· · · · ·) $\gamma T'_{\rm rms}/(\gamma-1)\overline{T}$.

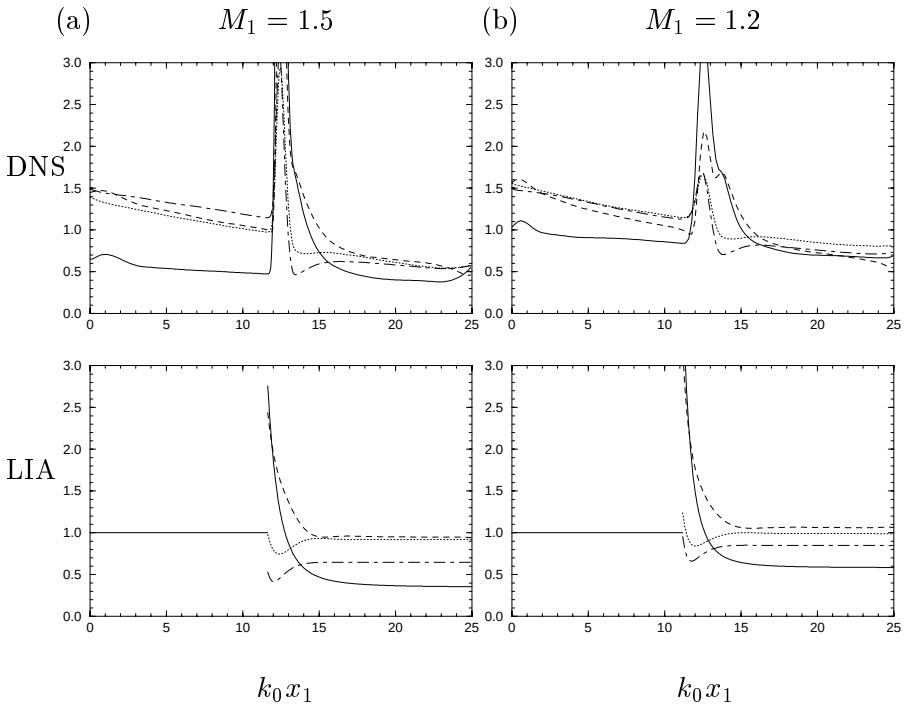

Figure 23. Evolution of rms values of the thermodynamic properties throughout the computational domain - DNS (up), I1.5ent (a) or I1.2ent (b) and LIA (down). All the curves are normalized by the value of $\rho'_{\rm rms}/\overline{\rho}$ immediately upstream of the shock. (——) $p'_{\rm rms}/\overline{p}$; (− − −) $\rho'_{\rm rms}/\overline{\rho}$; (· · · · ·) $T'_{\rm rms}/\overline{T}$; (− · −) $(\gamma-1)M_1^2\ u'_{1\,\rm rms}/U_1$.

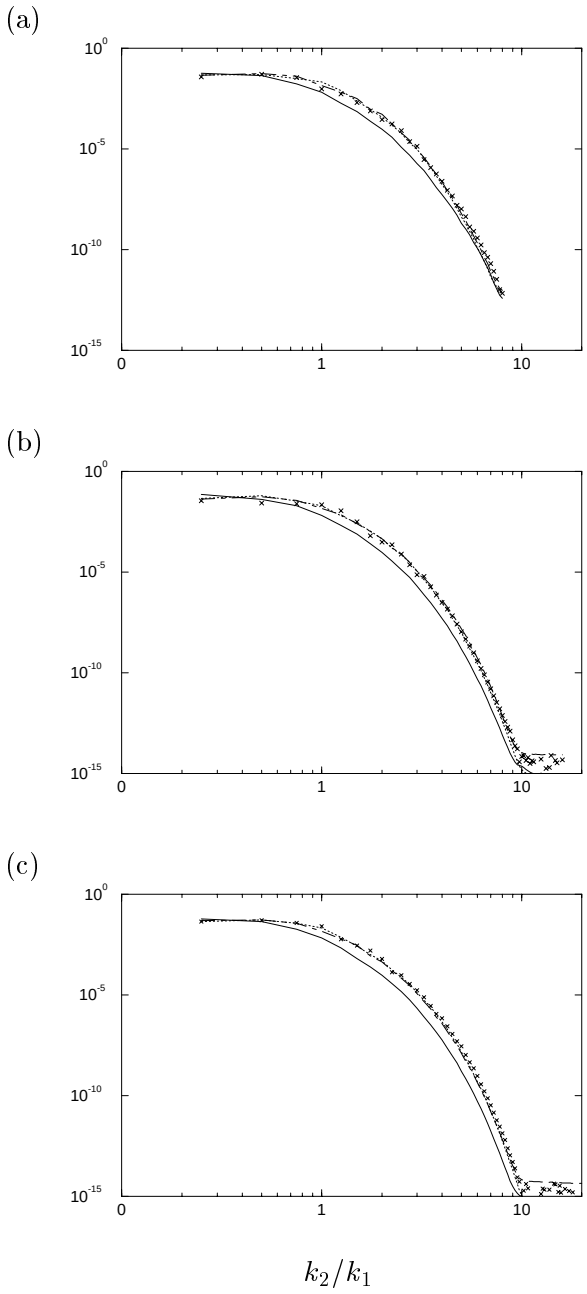

Figure 24. One-dimensional power spectra of velocity in the temporal simulations at $t/\tau_t = 0.75$. $M_1 = 1.5$, $u_0 = 1$, $k_0 = 4$, $\chi = 0$. 64^3 (a), 128^3 (b), 192^3 (c). ($- \cdot -$) $E_1(k_2)$; (——) $E_2(k_2)$; ($\cdots$) $E_3(k_2)$; ($\times \times \times$) $E_1(k_2)$ from $E_2(k_2)$ using equation (16).

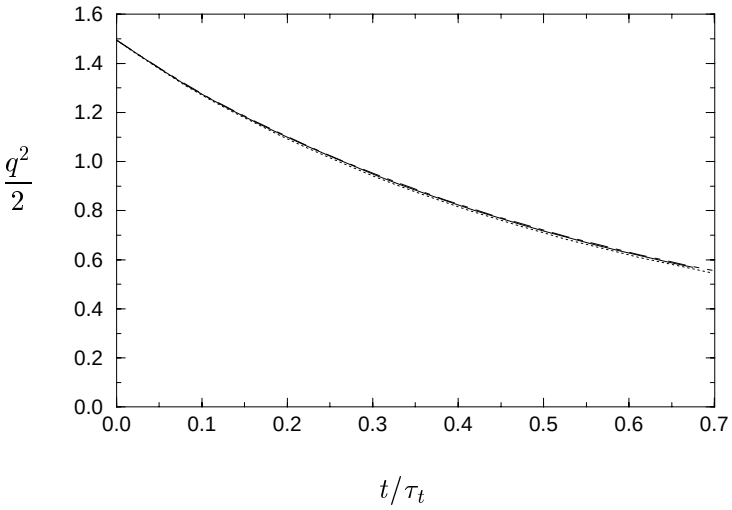

Figure 25. Evolution of the turbulent kinetic energy in the temporal decay of isotropic turbulence. $M_1 = 1.5$, $u_0 = 1$, $k_0 = 4$, $\chi = 0$. $(\cdots\cdots)$ 64^3; (——) 128^3; $(- \cdot -)$ 192^3.

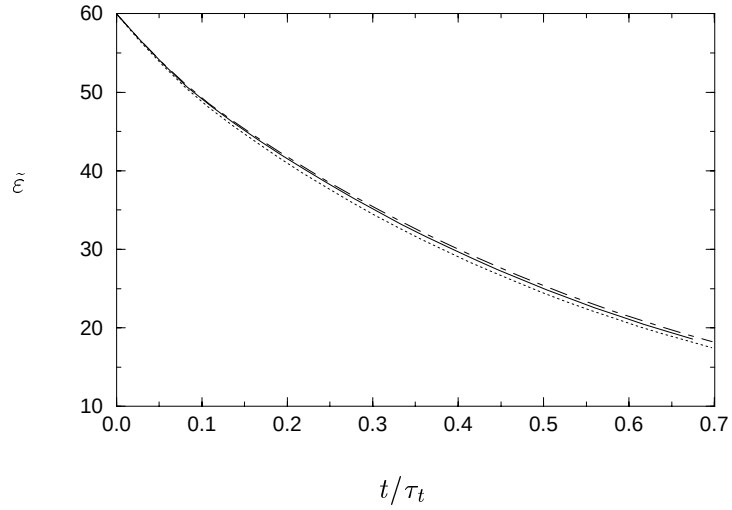

Figure 26. Evolution of the dissipation rate in the temporal decay of isotropic turbulence. $M_1 = 1.5$, $u_0 = 1$, $k_0 = 4$, $\chi = 0$. $(\cdots\cdots)$ 64^3; (——) 128^3; $(- \cdot -)$ 192^3.

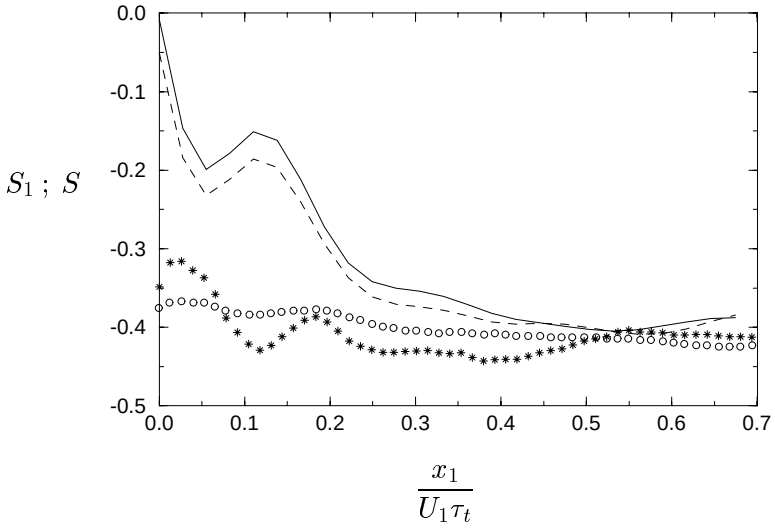

Figure 27. Evolution of the longitudinal (S_1) and mean (S) velocity derivative skewness in the simulations of isotropic, decaying turbulence. $M_1 = 1.5$. ($* * *$) S_1 spatial simulation; ($- - -$) S_1 temporal simulation with 128^3 grid points; ($\circ\circ\circ$) S spatial simulation; (——) S temporal simulation with 128^3 grid points.

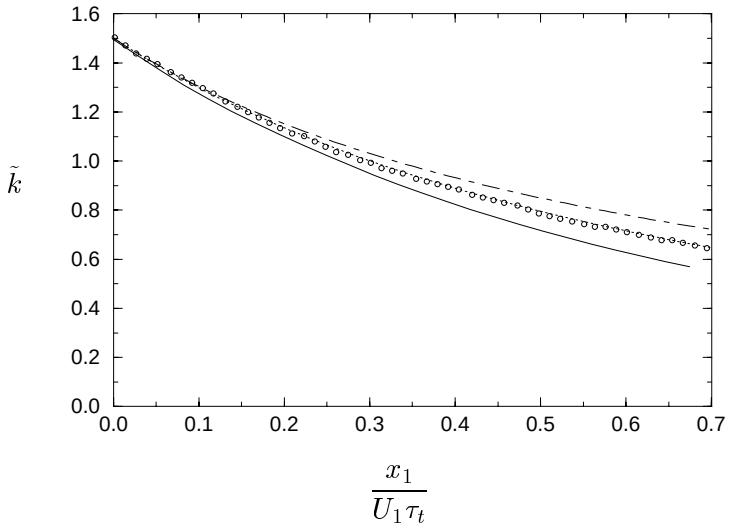

Figure 28. Evolution of the kinetic energy in the simulations of isotropic, decaying turbulence. $M_1 = 1.5$. ($\circ\ \circ\ \circ$) spatial simulation; (——) temporal simulation with 128^3 grid points; ($-\cdot-$) theory with $C_{\varepsilon_2} = 1.92$; ($\cdot\cdot\cdot\cdot\cdot$) theory with $C_{\varepsilon_2} = 1.5$.

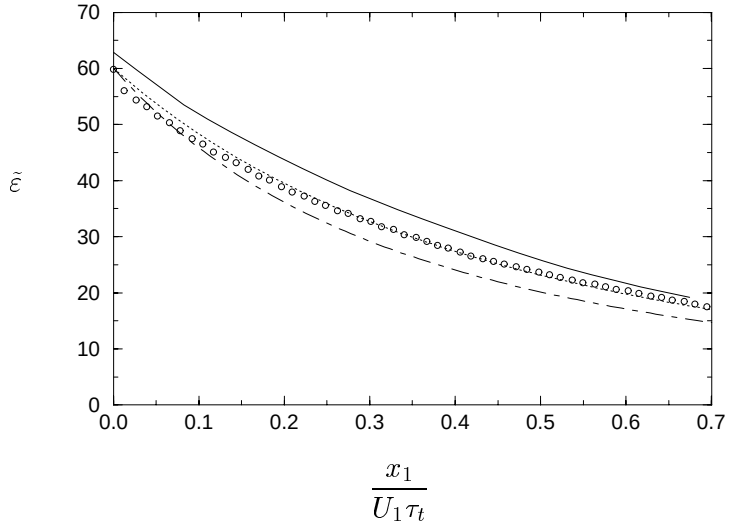

Figure 29. Evolution of the dissipation rate in the simulations of isotropic, decaying turbulence. $M_1 = 1.5$. ($\circ\ \circ\ \circ$) spatial simulation; (——) temporal simulation with 128^3 grid points; ($-\cdot-$) theory with $C_{\varepsilon_2} = 1.92$; ($\cdot\cdot\cdot\cdot\cdot$) theory with $C_{\varepsilon_2} = 1.5$.

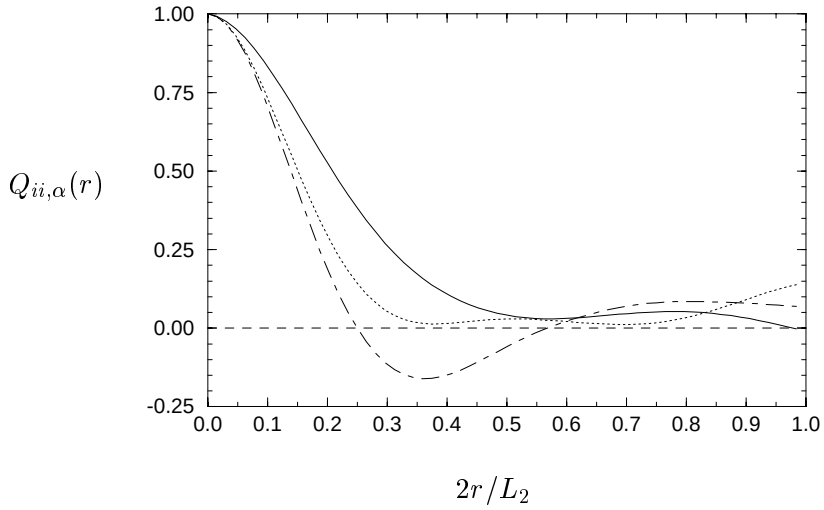

Figure 30. Two-points correlations in the $(x_1 = \pi)$ plane of the spatial simulation of isotropic, decaying turbulence. $(- \cdot -)$ $Q_{11,2}$; (——) $Q_{22,2}$; $(\cdot \cdot \cdot \cdot \cdot)$ $Q_{33,2}$.

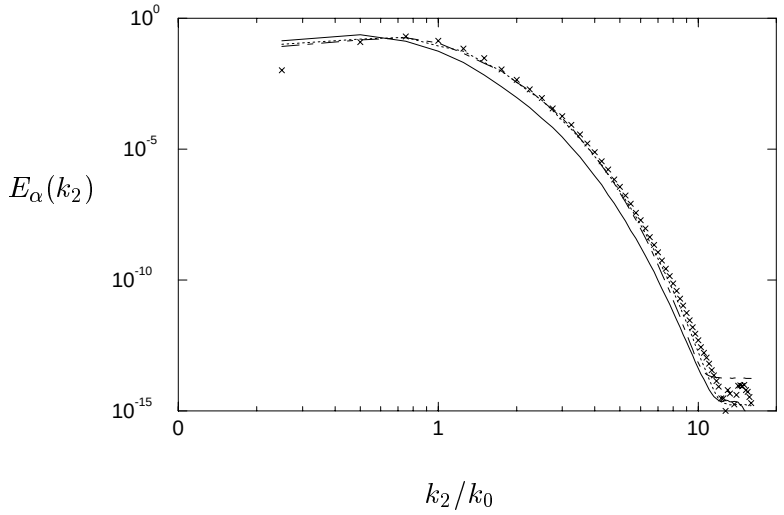

Figure 31. One-dimensional power spectra of velocity in the $(x_1 = \pi)$ plane of the spatial simulation of isotropic, decaying turbulence. $(- \cdot -)$ $E_1(k_2)$; (——) $E_2(k_2)$; $(\cdot \cdot \cdot \cdot \cdot)$ $E_3(k_2)$; $(\times \times \times)$ $E_1(k_2)$ from $E_2(k_2)$ using equation (16).

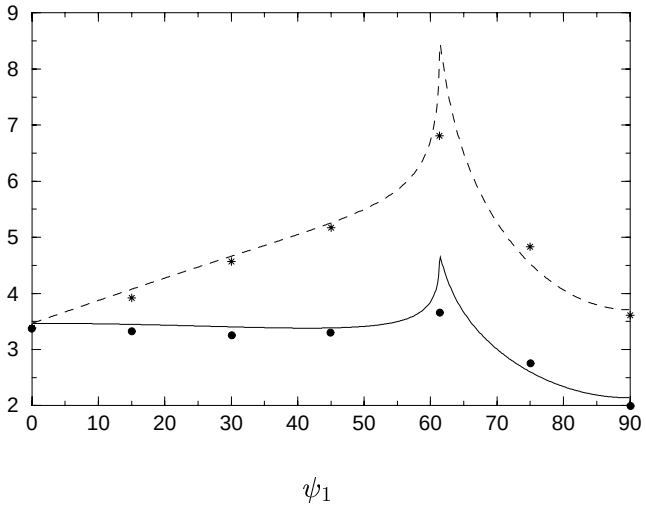

Figure 32. Amplification of vorticity ($\overline{\omega_2'^2}/\overline{\omega_1'^2}$) across the shock as a function of the angle of incidence - $M_1 = 1.5$. Comparison DNS/LIA : (——) LIA [$A_e = 0,\ A_v = 2.5\%$]; (•) DNS [$A_e = 0,\ A_v = 2.5\%$]; (– – –) LIA [$A_e = A_v = 2.5\%$]; (∗) DNS [$A_e = A_v = 2.5\%$].